PDS CAPS IMS Time-of-Flight (TOF) Analysis Procedures

Version: 1.0

Date: 21 August, 2019

Authors: H.T.Smith[1], F.J. Crary[2], D.B. Reisenfeld[3], M.D. Shappirio[4], E.C. Sittler[4], A.K. Woodson[5]

1. The Johns Hopkins University Applied Physics Laboratory, Laurel, Maryland. USA
2. Laboratory for Atmospheric and Space Physics, University of Colorado, Boulder, Colorado, USA
3. Los Alamos National Laboratory, Los Alamos, New Mexico, USA
4. NASA Goddard Space Flight Center, Greenbelt, Maryland USA
5 The University of Virginia, Charlottesville, Virginia USA

0. Table of Contents

1. Introduction

The purpose of this document is to provide a guide to the reduction and analysis of time-of-flight (TOF) data generated by the Cassini Plasma Spectrometer (CAPS) Ion Mass Spectrometer (IMS) which is one of three CAPS sensors.

Reduction of CAPS data is described in detail in the Cassini Plasma Spectrometer (CAPS) PDS User's Guide, Version 1.0 (2012 August 31), ID IO-AR-017 by Wilson et al. (referred to hereafter as Wilson et al.). It is essential reading for anyone attempting to reduce and analyze IMS data as it is more comprehensive than the present document with respect to its treatment of CAPS information other than IMS TOF analysis. The present document should be considered a companion to Wilson et al., which should be consulted for information on data files, data structure, and data processing that is not provided here (in particular Sections 8 and 10 regarding IMS TOF data).

The IMS is a complex instrument and the on-board compression that data undergoes between initial measurement and transmission to Earth further complicates analysis. Hence great care must be taken when applying the techniques described below.

2. IMS TOF Operation

The IMS is comprised of a toroidal top-hat electrostatic analyzer (ESA) coupled to a TOF spectrometer that combines a conventional straight-through (ST) mass analyzer with a reflectron mass analyzer employing a linear electric field (LEF) to reflect positive ions as illustrated in Figure 1. The ESA selects ions according to their energy per charge (E/Q) over a range of ~0.6 to ~50 keV/q with resolution $\Delta E/E \approx 17\%$, where q is the absolute value of the electron charge. Energy is scanned over 64 logarithmically-spaced steps every 4.0 seconds. The timing electronics measure ion TOF which is converted to ion mass per charge (M/Q) either in-flight (the ION data product) or on the ground using the TOF data product discussed in this document. A complete description of the CAPS instrument and TOF component can be found in Young et al. (2004), Cassini Plasma Spectrometer Investigation, *Space Science Reviews 114*, 1–112. Table 1 below contains a list of IMS specifications.

Ions enter the ESA through one of eight collimators that divide the IMS field-of-view into eight azimuthal bins of 8.3° x 20°. Ions admitted by the ESA are subsequently accelerated through a potential difference of -14.577 kV and into one of eight ultra-thin carbon foils (nominally 0.5 ug/cm^2 but actually ~2 μg/cm^2 due to adsorbed material) that are optically aligned with the entrance collimators. Molecular ions are completely dissociated in the carbon foils, and each atomic fragment exits in a positive, negative, or neutral charge state with energy proportional to its fraction of the mass of its parent molecular ion.
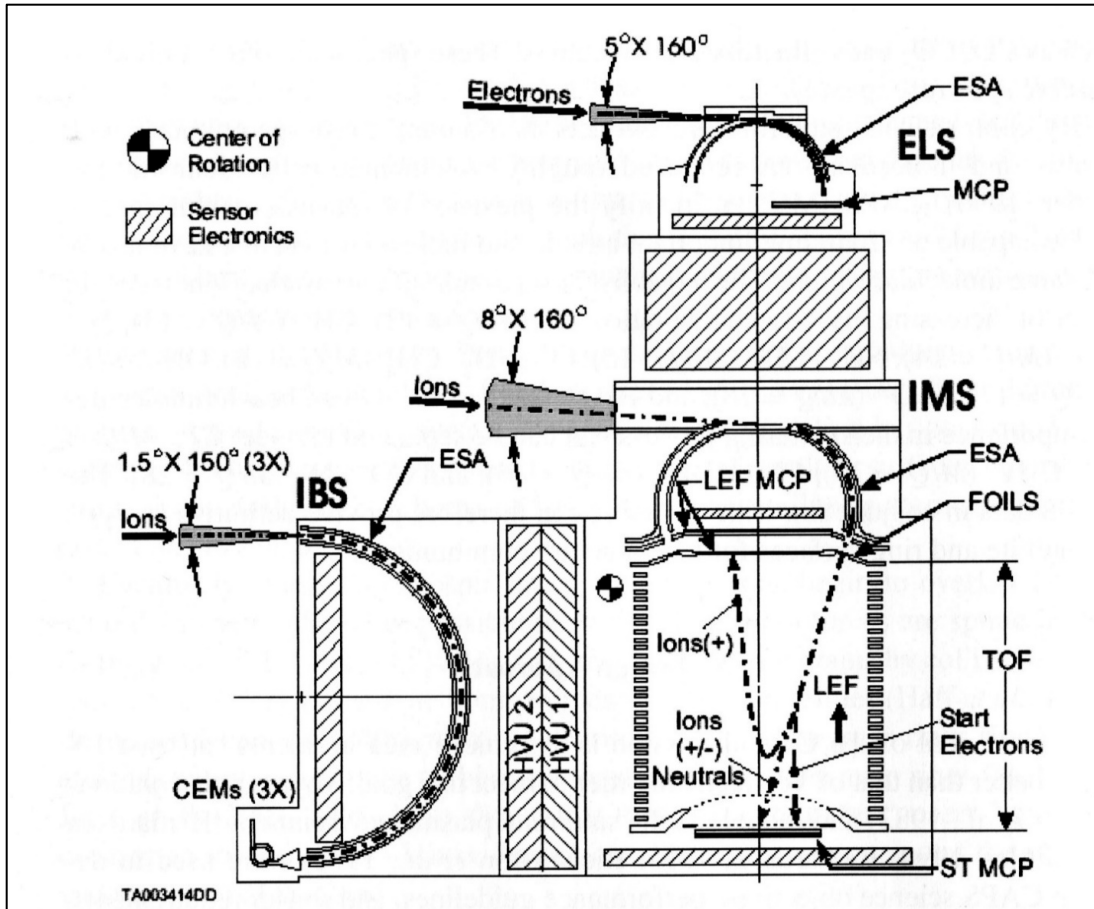
Figure 1. CAPS sensors cutaway with the fields-of-view shown in the azimuthal plane. Characteristic particle trajectories are shown schematically in the LEF region of the IMS.

Parameter	IMS ST	IMS LEF
Energy range (kV)	0.25 – 27.56	
Energy resolution (ΔE/E FWHM)	0.17	
Energy scan period	4.0 s	
Energy scan steps	64 log-spaced	
Analyzer constant FWHM (eV/V)	6.3	
Azimuth FWHM	8.3°	
Elevation FWHM	8 x 20°	
Mass range (energy dependent) (m/q)	0.3 - 400	0.1 - 54
Mass resolution (m/Δm FWHM)	≤ 5	≤ 40
Mass resolution (m/Δm @ 10% of peak)	≤ 15	≤ 85
Geometric factor (cm^2 sr eV/eV)*	1.5 x 10^{-3}	
Detection efficiency (counts/ion)	0.266	~0.03

Table 1. IMS performance specifications. *Note that ST and LEF geometric factors are set by the ESA optics and are the same. The count rates in the ST are lower than in the LEF because of differences in optical transmission through the LEF and in detector efficiency.

Electrons ejected from a foil by an incident molecular ion are accelerated through the linear electric field and strike the outer edge of the ST microchannel plate detector, generating a timer "start" signal in one of eight anodes corresponding to the 8.3° x 20° azimuthal channels. (Note that each "start" signal is counted as a "single" (SNG) event, such that nearly every ion admitted through the ESA is counted. Since SNG events do not require coincident start and stop signals to be counted, their detection efficiency is roughly an order of magnitude higher than that for TOF events.) Meanwhile, negative ion fragments, neutral ion fragments, and positively charged ion fragments with energies above ~16 keV travel "straight through" the linear electric field where they strike the center of the ST detector and nominally generate a "stop" signal that coincides with the start signal generated by the ejected electrons. Ions or neutrals giving rise to ST events are not time-focused so their time resolution and hence mass resolution is relatively low (M/ΔM ~ 8) compared to LEF events. However, the mass range is relatively large, encompassing molecular ions with mass per charge from 1 amu/q up through ~125 amu/q.

Positively charged ions with energies <16 keV, on the other hand, are reflected back toward the linear electric field microchannel plate detector by the time-focusing electric field, nominally generating a stop signal that coincide with the electron start signal (an LEF event). Such a correlated ST or LEF event yields a time-of-flight, T, which can then be converted to mass per charge using the notional equation $M/Q = 2(E/Q)(T/L)^2$, where L is the time-of-flight path length of 18.8 cm. The LEF optics are designed so that the ions undergo (nearly) simple harmonic motion. Ideally, the TOF is proportional to the square root of the ion's mass, regardless of its energy. Only those ions that pass through the ESA with a charge state of +1 q can produce LEF stop events, since more highly charged ions produce fragments with more than 16 keV energy due to the -14.557 keV post-ESA acceleration.

In practice the logic for identifying valid ST and LEF events is relatively complicated. In addition to valid combinations in which paired start and stop signals are detected within a fixed timing window, the logic must reject invalid combinations, e.g. a start with no stop, a stop with no start, etc. Invalid events arise either when penetrating electrons or very high ion fluxes within the IMS cause spurious start or stop signals, or when the ST detector fails to register a stop signal. On occasion, of course, these random events will result in correlations that show up as background counts in the TOF spectra.

3. Data Description

Some of the following information is restated from Wilson et al. In particular, details about data file structure and location can be found therein.

An "A-cycle" is the primary timing unit of CAPS observations. This is a 32 second integration period during which the three CAPS sensors sweep through their entire observed energy ranges multiple times. In order to improve statistics and minimize telemetry rates the TOF data is integrated into "B-cycles" which are sums of 8, 16, or 32 sequential A-cycles. The integration time of a B-cycle is variable based on the telemetry mode. Most B-cycles are 256 seconds (8 A-cycles) or 512 seconds (16 A-cycles) in length. Only a small amount of data was collected using a 1024 second B-cycle (32 A-cycles). Because of telemetry limitations TOF data is not generated during telemetry modes with rates <2 kbps. B-cycle duration is given by the

COLLAPSE_AND_DURATION field in the corresponding TOF_XXXXXXXXX_U3.DAT file, and can be verified by counting associated A-cycles in either SNG_XXXXXXXXX_U3.DAT or ANC_XXXXXXXXX_U3.DAT, where the string of 9 X's here represents a 4-digit year, followed by a 3-digit day of year, followed by a 2-digit hour of day as explained in Wilson et al.

TOF data comprises both ST data associated with the ST detector and LEF data associated with the LEF detector. A single record in a TOF_XXXXXXXXX_U3.DAT file (hereafter simply called a TOF data file) comprises 13 different fields and contains ST and LEF data acquired for a single energy step during a single B-cycle, along with supporting information needed to reconstruct the spectrum. Multiple such records can be arranged into 2D ST and LEF spectrograms showing the number of ion counts integrated over a given B-cycle per energy step (y-axis) and per TOF channel (x-axis). Counts associated with a particular TOF channel and energy step can then be assigned an M/Q using the model functions provided in Section 8. The name of each field and associated number of elements is given in Table 2. Complete information about each field including data type, size in bytes, number of elements, and valid value ranges can be found in the TOF_U3.FMT file, which is described in Wilson et al.

Field Name	Number of Elements
B_CYCLE_NUMBER	1
TIME	1
TELEMETRY_MODE	1
COLLAPSE_AND_DURATION	1
ST_START_CHANNEL	1
ST_INTERVAL	1
ST_ENERGY COLLAPSE	1
LEF_START_CHANNEL	1
LEF_INTERVAL	1
LEF_ENERGY_COLLAPSE	1
ENERGY_STEP	1
DATA_ST	512
DATA_LEF	512

Table 2. Name and associated number of elements for each field in TOF data files.

Ion counts were collected in all 2048 TOF channels during flight. However, due to telemetry limitations only 512 representative values were transmitted to Earth per B-cycle per energy step for each of the ST and LEF detectors. The arrays containing these values are found in the DATA_ST and DATA_LEF fields in the TOF data files. Each array represents a selection of 512 equally-spaced channels from the full 2048, and these 512 selected channels may have been further collapsed after selection by summing or averaging within consecutive intervals of equal length. This process replaces the first element of each interval with the sum or average and sets the rest of the elements in the interval to MISSING_CONSTANT as defined in TOF_U3.FMT. In addition to B-cycle duration, COLLAPSE_AND_DURATION specifies whether these intervals have been summed or averaged. The interval length is determined by counting the number of MISSING_CONSTANT values following each valid value in the DATA_ST and DATA_LEF arrays. If there are no MISSING_CONSTANT values then no summing or averaging was performed.

Before mapping the 512 values in DATA_ST and the 512 values in DATA_LEF back to the full 2048-channel range, the MISSING_CONSTANT and collapsed values in those arrays must first be replaced with appropriate counts. Consider the example below, where the first element and every subsequent 4th element of DATA_ST are valid count values (c_0, c_4, c_8, ..., c_{508}) while all other elements are equal to MISSING_CONSTANT:

(1)

DATA_ST[0] = c_0,
DATA_ST[1] = DATA_ST[2] = DATA_ST[3] = MISSING_CONSTANT,

DATA_ST[4] = c_4,
DATA_ST[5] = DATA_ST[6] = DATA_ST[7] = MISSING_CONSTANT,

DATA_ST[8] = c_8,
DATA_ST[9] = DATA_ST[10] = DATA_ST[11] = MISSING_CONSTANT,
$$\vdots$$
DATA_ST[508] = c_{508},
DATA_ST[509] = DATA_ST[510] = DATA_ST[511] = MISSING_CONSTANT.

If COLLAPSE_AND_DURATION indicates that counts were summed then the values in DATA_ST would be replaced as follows:

(2)

DATA_ST[0] = DATA_ST[1] = DATA_ST[2] = DATA_ST[3] = c_0 / 4,

DATA_ST[4] = DATA_ST[5] = DATA_ST[6] = DATA_ST[7] = c_4 / 4,

DATA_ST[8] = DATA_ST[9] = DATA_ST[10] = DATA_ST[11] = c_8 / 4,
$$\vdots$$
DATA_ST[508] = DATA_ST[509] = DATA_ST[510] = DATA_ST[511] = c_{508} / 4.

If COLLAPSE_AND_DURATION instead indicates that the counts in each interval were averaged, then c_i / 4 would be replaced with $c_i \times 4$ in equation (2). The MISSING_CONSTANT and reduced values in DATA_LEF are replaced in the same manner.

Once the MISSING_CONSTANT and collapsed values have been replaced with appropriate counts, the 512 counts can be mapped to their absolute channel numbers (between 0 and 2047 inclusive) within the full 2048-channel spectrum. This is done using the ST_START_CHANNEL and ST_INTERVAL fields from the TOF data file for the DATA_ST array, and the LEF_START_CHANNEL and LEF_INTERVAL fields for the DATA_LEF array. The absolute channel corresponding to DATA_ST[i] is given by ST_START_CHANNEL + $i \times$ ST_INTERVAL, and that corresponding to DATA_LEF[i] is given by LEF_START_CHANNEL + $i \times$ LEF_INTERVAL, where $i = 0, 1, 2, ..., 511$. In most cases the 2048-channel ST spectra were sampled at every other channel starting with channel 40 and

ending at channel 1064. LEF spectra acquired inside ~ 23 Saturn radii (Rs) start at channel 650 and include every consecutive channel up to and including 1162, while LEF spectra acquired farther out than about 23 Rs usually start at channel 40 and include every consecutive channel up to and including channel 552. This strategy was adopted based on the initial spacecraft orbits at Saturn to optimize LEF data for the dominant mass range of each region. However, this strategy was not always applied. Initially, the default was to sample every fourth channel over the full TOF range, and prior to DOY 58, 2005, both LEF and ST data started at channel 40 and recorded at every 4th channel. Therefore, the channel selection strategy for each spectrum should be verified using the above information.

While CAPS SNG counts are partitioned into 63 energy bins corresponding to the 63 energy levels swept by the ESA (omitting the 64th fly-back step of the sweep), CAPS TOF data is collapsed into 32 energy bins using one of three methods: 1) only even-indexed energy levels are selected, 2) only odd-indexed energy levels are selected, or 3) the counts associated with adjacent energy level pairs are summed. For a given TOF record the ENERGY_STEP field provides the bin index, between 1 and 32 inclusive, and the ST_ENERGY_COLLAPSE and LEF_ENERGY_COLLAPSE fields indicate the collapse method that was used. The most common energy collapse used for the TOF data is adjacent energy-channel summing, for which ENERGY_STEP = 1 corresponds to the first energy level (index 1) of the ESA sweep (not summed with any other channel) and the next 62 ESA energy levels are then summed in pairs (see Wilson et al. for further elaboration).

Table 3 shows the ESA sweep tables used before June 11, 2007 (1st and 3rd columns) and after June 11, 2007 (2nd and 4th columns) at distances greater than 2000 km from Titan (1st and 2nd columns) and less than 2000 km from Titan (3rd and 4th columns). The sweep table used for a particular TOF record is identified by the SWEEP_TABLE_NUMBER field in the ANC data file that has the same time stamp as the TOF data file containing the record. The SWEEP_TABLE_NUMBER references the sweep table file on the PDS that has the same number in its filename. In the ANC data files, each record coincides with a 32-second A-cycle, so there are multiple records for each B-cycle. In most cases all ANC records with the same B_CYCLE_NUMBER, or with TIME fields that fall within the duration of the same B-cycle, will have the same SWEEP_TABLE_NUMBER. Note that the sweep table files available on the PDS are actually ESA voltage tables, and each voltage must be multiplied by a conversion factor of 6.3 (see Table 1) in order to obtain the energies shown in Table 3.

There are periods during which A-cycle and B-cycle time stamps are misaligned due to an on-board data buffering glitch that occurs for some telemetry changes, so the user should check that the SWEEP_TABLE_NUMBER does not vary from A-cycle to A-cycle within the same B-cycle (although certain small variations are permissible as noted on page 88 of Wilson et al.). These offsets are also important to consider when correlating TOF spectra with their concurrent SNG spectra in order to gauge temporal and spatial variations in the plasma, and variations in instrument pointing, over the course of a TOF integration period.

Index	IMS_SWEEP_TABLE_1_Std.DAT ESA Voltage (V)	Ion E/Q (eV)	IMS_SWEEP_TABLE_2_Std.DAT ESA Voltage (V)	Ion E/Q (eV)	IMS_SWEEP_TABLE_15_Std.DAT ESA Voltage (V)	Ion E/Q (eV)	IMS_SWEEP_TABLE_17_Std.DAT ESA Voltage (V)	Ion E/Q (eV)
1	7415.00	46343.76	5243.40	32771.22	7415.00	46343.75	5243.92	32774.50
2	6234.40	38964.97	5243.40	32771.22	7415.00	46343.75	5243.92	32774.50
3	5243.40	32771.22	5243.40	32771.22	6234.40	38965.00	5243.92	32774.50
4	4409.16	27557.28	4409.16	27557.28	5243.92	32774.50	4409.16	27557.25
5	3706.60	23166.22	3706.60	23166.22	4409.16	27557.25	3706.60	23166.25
6	3118.10	19488.14	3118.10	19488.14	3706.60	23166.25	3118.10	19488.13
7	2621.96	16387.24	2621.96	16387.24	3118.10	19488.13	2621.96	16387.25
8	2203.68	13772.98	2203.68	13772.98	2621.96	16387.25	2203.68	13773.00
9	1854.20	11588.77	1854.20	11588.77	2203.68	13773.00	1854.20	11588.75
10	1559.05	9744.07	1559.05	9744.07	1854.20	11588.75	1559.05	9744.06
11	1310.98	8193.62	1310.98	8193.62	1559.05	9744.06	1310.98	8193.63
12	1102.74	6892.15	1102.74	6892.15	1310.98	8193.63	1102.74	6892.13
13	927.10	5794.38	927.10	5794.38	1102.74	6892.13	927.10	5794.38
14	778.62	4866.38	778.62	4866.38	927.10	5794.38	778.62	4866.38
15	655.49	4096.81	655.49	4096.81	778.62	4866.38	655.49	4096.81
16	550.47	3440.42	550.47	3440.42	655.49	4096.81	550.47	3440.44
17	463.55	2897.19	463.55	2897.19	550.47	3440.44	463.55	2897.19
18	389.31	2433.19	389.31	2433.19	463.55	2897.19	389.31	2433.19
19	327.74	2048.41	327.74	2048.41	389.31	2433.19	327.74	2048.38
20	275.23	1720.21	275.23	1720.21	327.74	2048.38	275.23	1720.19
21	231.78	1448.60	231.78	1448.60	275.23	1720.19	231.78	1448.63
22	194.85	1217.79	194.85	1217.79	231.78	1448.63	194.85	1217.81
23	163.82	1023.90	163.82	1023.90	194.85	1217.81	163.82	1023.88
24	137.80	861.23	137.80	861.23	163.82	1023.88	137.80	861.25
25	115.86	724.13	115.86	724.13	137.80	861.25	115.86	724.13
26	97.40	608.75	97.40	608.75	115.86	724.13	97.40	608.75
27	81.94	512.10	81.94	512.10	97.40	608.75	81.94	512.13
28	68.90	430.61	68.90	430.61	81.94	512.13	68.90	430.63
29	57.91	361.92	57.91	361.92	68.90	430.63	57.91	361.94
30	48.72	304.52	48.72	304.52	57.91	361.94	48.72	304.50
31	40.97	256.05	40.97	256.05	48.72	304.50	40.97	256.06
32	34.45	215.31	34.45	215.31	40.97	256.06	34.45	215.31
33	28.98	181.11	28.98	181.11	34.45	215.31	28.98	181.13
34	24.36	152.26	24.36	152.26	28.98	181.13	24.36	152.25
35	20.46	127.88	20.46	127.88	24.36	152.25	20.46	127.88
36	17.22	107.65	17.22	107.65	20.46	127.88	17.22	107.63
37	14.46	90.41	14.46	90.41	17.22	107.63	14.46	90.38
38	12.18	76.13	12.18	76.13	14.46	90.38	12.18	76.13
39	10.23	63.94	10.23	63.94	12.18	76.13	10.23	63.94
40	8.61	53.83	8.61	53.83	10.23	63.94	8.61	53.81
41	7.23	45.20	7.23	45.20	8.61	53.81	7.23	45.19
42	6.09	38.07	6.09	38.07	7.23	45.19	6.09	38.06
43	5.12	32.00	5.12	32.00	6.09	38.06	5.12	32.00
44	4.30	26.91	4.30	26.91	5.12	32.00	4.30	26.88
45	3.62	22.63	3.62	22.63	4.30	26.88	4.30	26.88
46	3.04	19.03	3.04	19.03	4.30	26.88	4.30	26.88
47	2.56	16.00	2.56	16.00	4.30	26.88	4.30	26.88
48	2.15	13.46	2.15	13.46	4.30	26.88	4.30	26.88
49	1.81	11.32	1.81	11.32	4.30	26.88	4.30	26.88
50	1.52	9.51	1.52	9.51	4.30	26.88	4.30	26.88
51	1.28	8.00	1.28	8.00	4.30	26.88	4.30	26.88
52	1.08	6.73	1.08	6.73	4.30	26.88	4.30	26.88
53	0.91	5.66	0.91	5.66	4.30	26.88	4.30	26.88
54	0.76	4.76	0.76	4.76	4.30	26.88	4.30	26.88
55	0.64	4.00	0.64	4.00	4.30	26.88	4.30	26.88
56	0.54	3.36	0.54	3.36	4.30	26.88	4.30	26.88
57	0.45	2.83	0.45	2.83	4.30	26.88	4.30	26.88
58	0.38	2.38	0.38	2.38	4.30	26.88	4.30	26.88
59	0.32	2.00	0.32	2.00	4.30	26.88	4.30	26.88
60	0.27	1.68	0.27	1.68	4.30	26.88	4.30	26.88
61	0.23	1.41	0.23	1.41	4.30	26.88	4.30	26.88
62	0.19	1.19	0.19	1.19	4.30	26.88	4.30	26.88
63	0.00	0.00	0.00	0.00	4.30	26.88	4.30	26.88

Table 3. CAPS ESA sweep tables. Tables 1 and 2 were used at distances > ~2000 km from Titan, and tables 15 and 17 at distances < ~2000 km from Titan. Tables 1 and 15 were used before 11 June 2007, and tables 2 and 17 were used after 11 June 2017. Ion E/Q = ESA Voltage × 6.3.

4. Data Processing Considerations

In order to extract peak shapes from reconstructed spectra the user must first remove instrument noise and background signals from each spectrum. The instrument noise is called Repeating Pattern Noise and takes the form of a repeating pattern of spikes and pits that will be discussed in more detail below. Figures 2, 3, and 4 illustrate how different ambient environments affect IMS background levels. Figures 2 and 3 show IMS ST and LEF spectrograms while Figure 4 shows an anode-averaged IMS SNG spectrum taken from Hill et al. 2012. The data in figures 2 and 3 are summed over 6-hour periods and represent normal S/N and high background with low S/N cases, respectively. The data in Figure 4 were collected during Enceladus flyby E3. Note how the high, diffuse background largely disappears over the course of a single TOF integration period during passage through the moon's corotational wake. This emphasizes the importance of characterizing TOF background on a per B-cycle basis whenever possible.
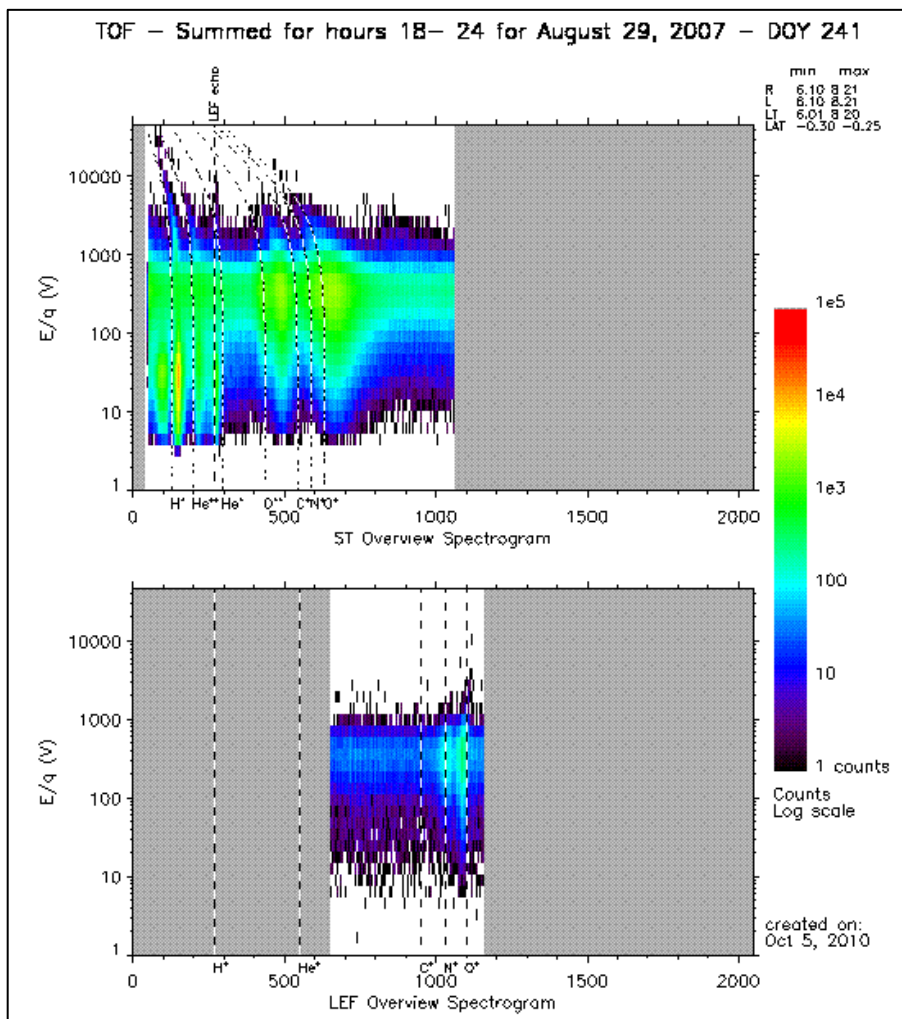

Figure 2. Example of high signal-to-noise IMS ST (top) and LEF (bottom) spectrograms showing total counts summed over a six-hour period as a function of energy-per-charge (Y-axis) and TOF channel (X-axis).

Each TOF spectrum should be processed separately when sufficiently resolved as the background signal varies with time, energy step and TOF channel. Care should be taken when summing spectra over multiple energy steps to enhance signal. It is relatively safe to sum LEF spectra over multiple energy steps since LEF peak locations do not vary appreciably with energy due to time-focusing. However, LEF peak widths have a second-order energy dependence so summing over energy steps may result in artificially widened peaks. ST peak positions, on the other hand, vary appreciably with ion energy above ~200 eV (note the shapes of the dashed lines in the top panel of Figure 2, for example) so sums should be restricted to low energies (< ~200 eV) or similar energies over multiple B-cycles. When summing over multiple B-cycles additional care must be taken to ensure that ST(LEF)_START_CHANNEL and ST(LEF)_INTERVAL are the same for all summed B-cycles.
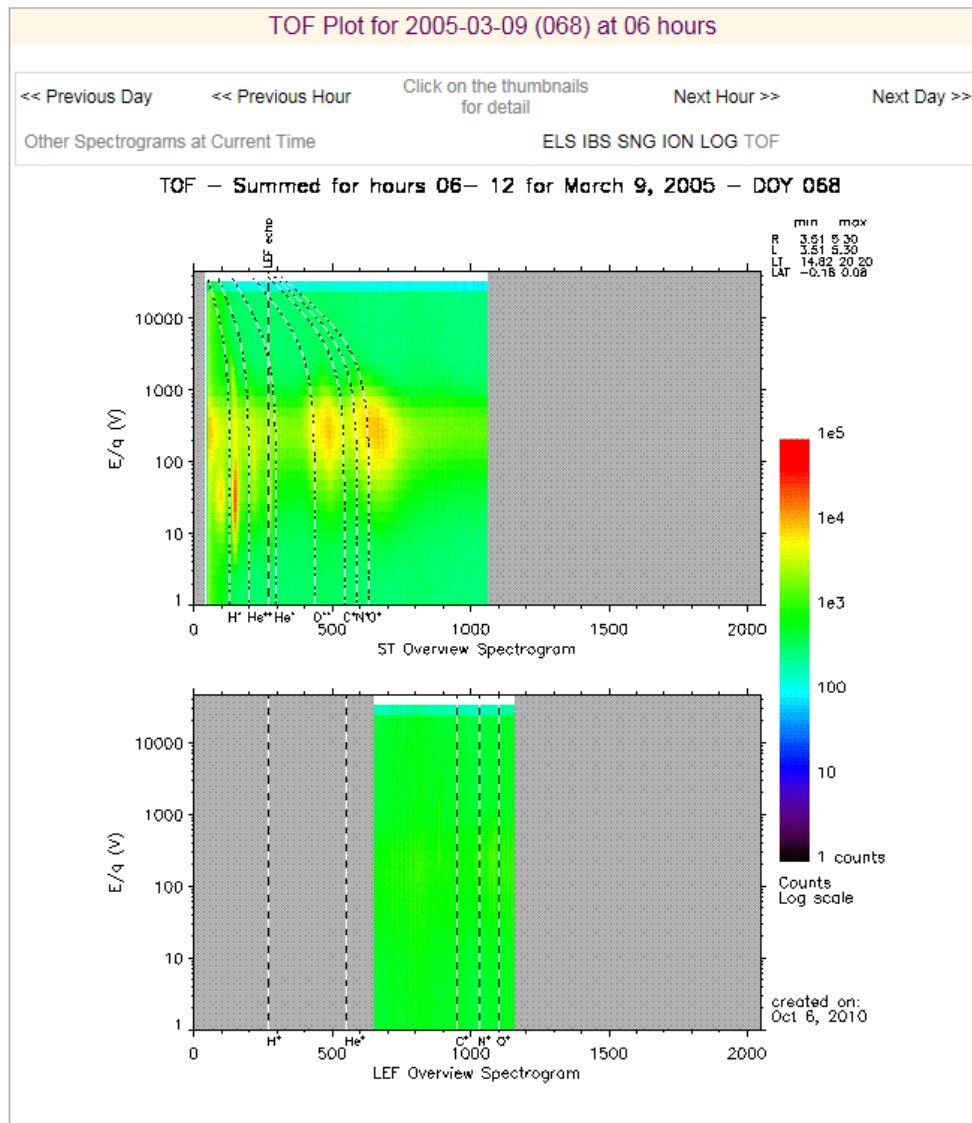

Figure 3. Example of low signal-to-noise ST (top) and LEF (bottom) spectrograms showing total counts summed over a 6-hour period as a function of energy-per-charge and TOF channel.

ST and LEF spectra are subject to 1) instrument noise caused by a glitch in the IMS timing electronics and 2) background signal produced by penetrating electrons and high ion fluxes. MeV electrons can penetrate the IMS walls and reach the MCP detectors where they generate erroneous start and stop signals, sometimes at very high rates. Trapped radiation closer than 4 Rs from Saturn is a common source of these penetrating electrons. High background levels can also be caused by excessive ion fluxes encountered during flybys at low altitudes near Titan and Enceladus where plasma densities can be very high. In these environments ions and electrons enter the IMS at such a high rate that the instrument is overwhelmed by secondary scattered particles and electrons ejected from the foils by incident molecular ions can no longer be correlated with those ions. For example, two electrons might strike the outer start and inner stop sections of the ST MCP in rapid succession before an ion fragment reaches the stop section. The stop electron in this scenario could be a penetrating electron or a secondary electron produced by an ion fragment that strikes a surface inside the IMS. Such events generate spurious coincidences along the TOF continuum, and in high-flux environments the result is a relatively smooth and well-resolved background shape.

The Repeating Pattern Noise (RPN), on the other hand, is caused by impedance mismatches along the physical delay line used in the IMS timing circuitry. These mismatches result in a non-uniform "tick-length" along the 16 taps of the delay line, where each tick corresponds to the duration of a single TOF channel (nominally 0.781 ns). Thus, ions detected near the boundaries between consecutive ticks may be improperly binned in a manner that repeats every 16 TOF channels. The pattern is not well resolved in low-count spectra but becomes clear in high-flux environments or when summing spectra, as shown in Figure 5.
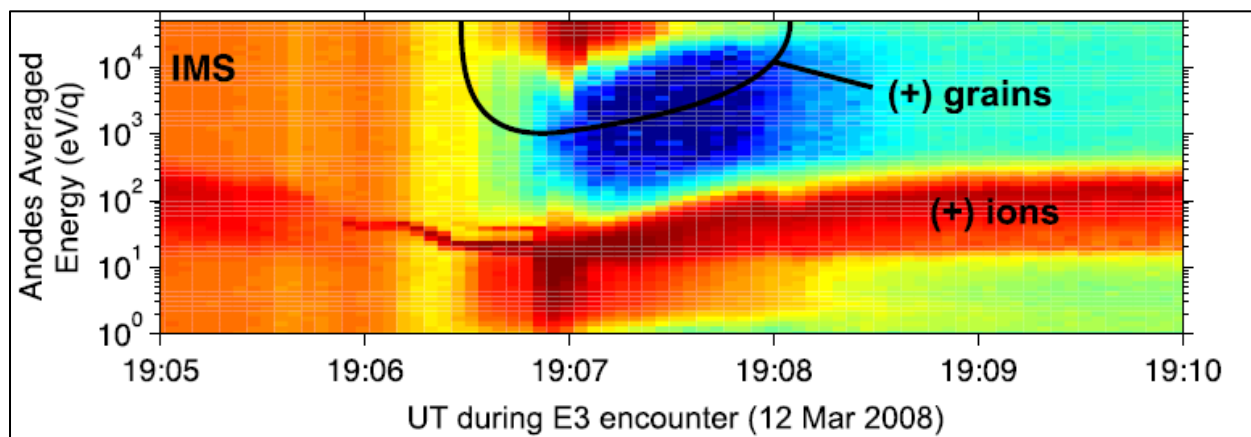

Figure 4. Example of a complex SNG spectrum illustrating strong variation in IMS background levels within the duration of a single TOF integration period (i.e. B-cycle). This highlights the importance of selecting background levels on a B-cycle by B-cycle basis. The figure is taken from Hill et al., 2012.

5. Repeating Pattern Noise Reduction

The simplest way to approximate RPN removal from a given spectrum is to apply a smoothing filter such as a boxcar average or a Savitzky-Golay filter. However, this method requires that the spectrum be sufficiently resolved so that the values within the filter window vary, more or less,

about the true distribution. The top panel of Figure 5 shows the RPN emerging from a raw, low signal-to-noise LEF spectrum that has been summed over multiple energy bins and B-cycles to enhance the signal. Since the LEF peak locations are not sensitive to ion energy and the RPN does not appear to vary over time (see Section 6 below), summing LEF spectra over multiple energy bins and/or B-cycles often yields a highly resolved LEF spectrum from which the RPN can be effectively removed. For example, the middle panel in Figure 5 shows the result of applying a boxcar average with a window size of 5 TOF bins to the spectrum in the top panel. As discussed earlier, care should be taken when summing spectra to ensure that the ST(LEF)_START_CHANNEL and ST(LEF)_INTERVAL values are the same for all summed spectra, and that the TOF peak locations do not vary appreciably over the energy range summed. This method is therefore more effective for RPN removal from LEF spectra than for ST spectra.

A second and more accurate method of reducing RPN involves extracting an average 16-channel pattern from a representative LEF spectrum and then applying a correction, based on this average pattern, to each 16-channel interval of a target spectrum. Although the lower efficiency of the LEF detector yields significantly fewer LEF counts as compared to the ST detector (e.g. Figures 2 and 3), there are a couple of reasons for using LEF spectra acquired in high-flux environments (e.g. at low Titan altitudes) to extract the pattern. First, most LEF spectra comprise 512 contiguous TOF channels out of the full range of 2048 channels while ST spectra typically comprise every other or every 4th channel depending on instrument mode. Thus it is not possible to characterize the full, contiguous 16-channel pattern using ST spectra due to missing values. Second, high ion and electron fluxes result in a high, fairly uniform, linear LEF background from which the repeating pattern can be extracted. In contrast, the analogous background in the ST spectrum takes an exponential shape at low TOF channels because scattered electrons, which are repelled from the LEF detector and attracted to the ST detector, have very short TOF within the linear electric field.

Figure 6 illustrates the process of extracting the repeating pattern from LEF spectra acquired within 2200 km of Titan at energies between 20 eV and 30 eV. The top panel shows the sum of these spectra over a 26-month period from October 2004 to December 2006, the middle panel over a 12 month period from January 2008 to December 2008, and the bottom panel over a 9-month period from February 2009 to October 2009. The sums in these cases were each restricted to a single energy bin as part of a systematic study. In general, though, LEF spectra can be summed over energy provided the previously discussed precautions are taken.

The first step in extracting the repeating pattern with this method is to fit a straight line to the representative LEF spectrum. In the three cases in Figure 6 gray bars labeled "PTRN" just above the x-axis indicate the channels selected for fitting, and solid black lines indicate the fits. The upper and lower bounds of each 16-channel interval are indicated by light gray grid lines. In all there are 2048 / 16 = 128 16-channel intervals covering the full range of TOF channels. In these examples the half-full 16-channel intervals at either end of the data range have been omitted from the average, but partially-full intervals can be included as long as a separate summand count is maintained for each of the 16 sums comprising the average pattern.
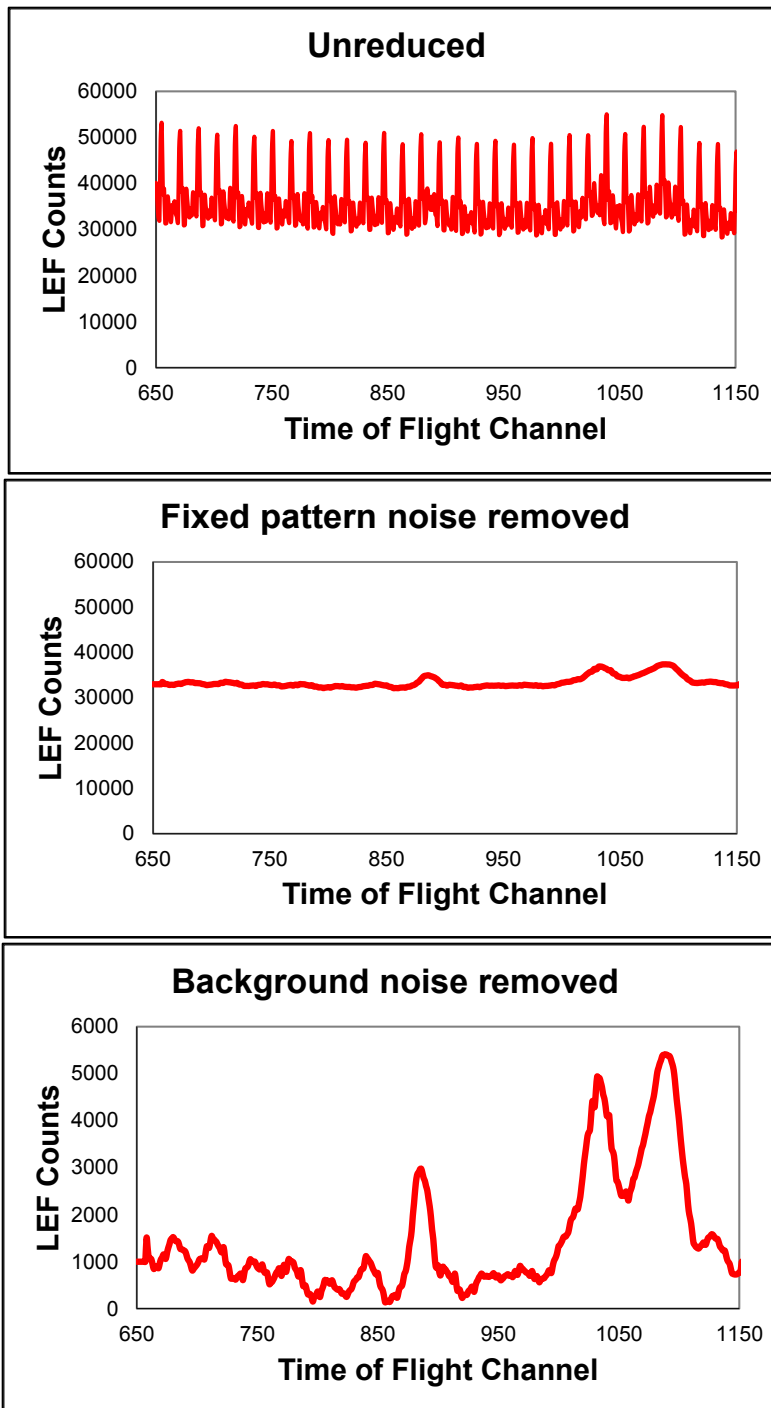
Figure 5. Raw LEF spectrum (DOY 68, 2005). LEF ion counts vs. TOF channel shown with background and repeating pattern noise (top), with repeating pattern noise reduced (middle), and with repeating pattern noise reduced and background subtracted (bottom).
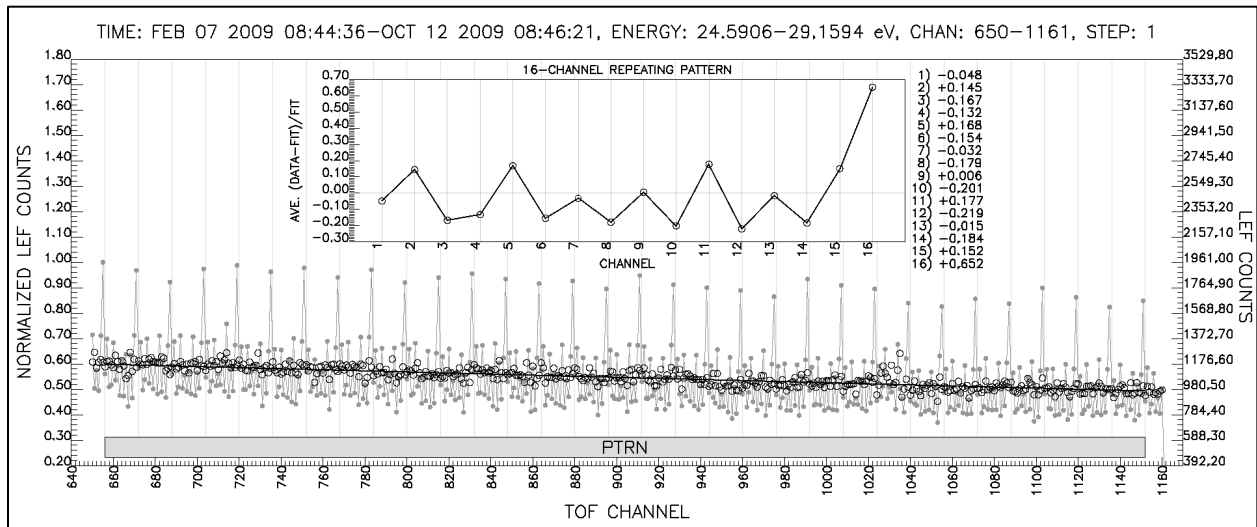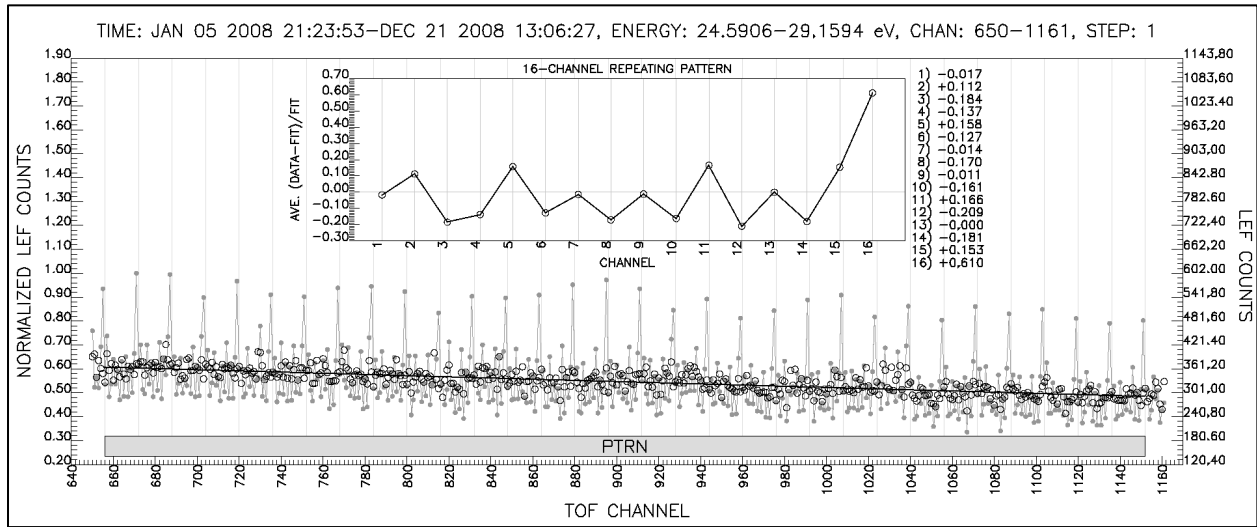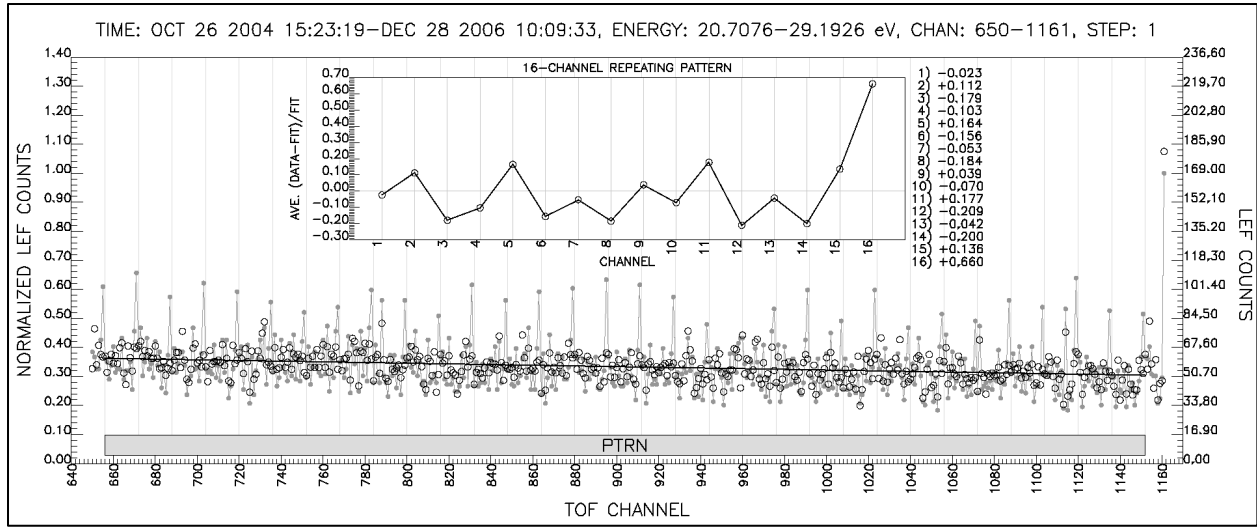
Figure 6. Characterization of RPN using summed LEF spectra. The 16-channel patterns extracted from the spectra are shown in the insets. Filled gray circles represent the summed raw data and open black circles represent the pattern-corrected data.

Next the relative difference between the spectrum and the fitted line is calculated for each data point:

$$\text{(3)} \qquad r_i = (c_i - f_i) / f_i$$

where c_i represents the count at channel i and f_i represents the value of the fitted line at channel i. These relative differences are then averaged over consecutive 16-channel intervals to obtain the average pattern:

$$\text{(4)} \qquad \{\bar{r}_0, \bar{r}_1, \bar{r}_2, ..., \bar{r}_{15}\} = \sum_{j=0}^{127} \left\{ \frac{r_{j\times16+0}}{N_0}, \frac{r_{j\times16+1}}{N_1}, \frac{r_{j\times16+2}}{N_2}, ..., \frac{r_{j\times16+15}}{N_{15}} \right\}$$

where j is the interval index and N_0, N_1, ..., N_{15} are the summand counts for each of the 16 sums comprising the average pattern,

$$\text{(5)} \qquad N_k = \sum_{j=0}^{127} \begin{cases} 1 & \text{if } c_{j\times16+k} \text{ was selected from the full range of 2048 channels} \\ 0 & \text{otherwise} \end{cases}.$$

The average patterns calculated for the three cases in figure 6 are shown in the insets.

Finally, applying the pattern correction to a given LEF or ST spectrum is equivalent to replacing the counts $\{c_{j\times16+0}, c_{j\times16+1}, c_{j\times16+2}, ..., c_{j\times16+15}\}$ in each consecutive 16-channel subinterval with the 16 values $\{f_{j\times16+0}, f_{j\times16+1}, f_{j\times16+2}, ..., f_{j\times16+15}\}$ obtained from the relative difference formula. In other words:

$$\text{(6)} \qquad f_{j\times16+k} = c_{j\times16+k}/(\bar{r}_k + 1)$$

for j = 0, 1, 2, ..., 127 and k = 0, 1, 2, ... 15. Recall that each TOF spectrum comprises a subset of the total 2048 TOF channels and so those channels that are not represented in a given spectrum (i.e. $c_{j\times16+k}$ was not selected) should be skipped in the above sums and when applying the pattern correction. In figure 6 filled gray circles represent the summed raw data and open black circles represent the corrected data. After applying the pattern correction a smoothing filter may be used to further reduce the point spread as in the first RPN-removal method described above.

A mission-long analysis of LEF spectra summed over 5 different 1- to 3-year periods between October 2004 and May 2012, including the three represented in Figure 6, confirms that the pattern changes very little over the course of the mission. This result is shown in Figure 7. However, it is important to note that the efficacy of this method increases with ion count statistics. As an example, notice that the correction reduces point spread considerably more in the bottom panel of Figure 6, which has roughly 20 times more signal than the top panel. Thus, the pattern should only be extracted from LEF spectra with sufficient ion count accumulation, which generally necessitates a sum over spectra. A pattern extracted from a poorly resolved spectrum will be a poor approximation to the true pattern. Likewise, the pattern correction should only be

applied to well-resolved LEF and ST spectra. Otherwise the correction may introduce more noise than it removes.
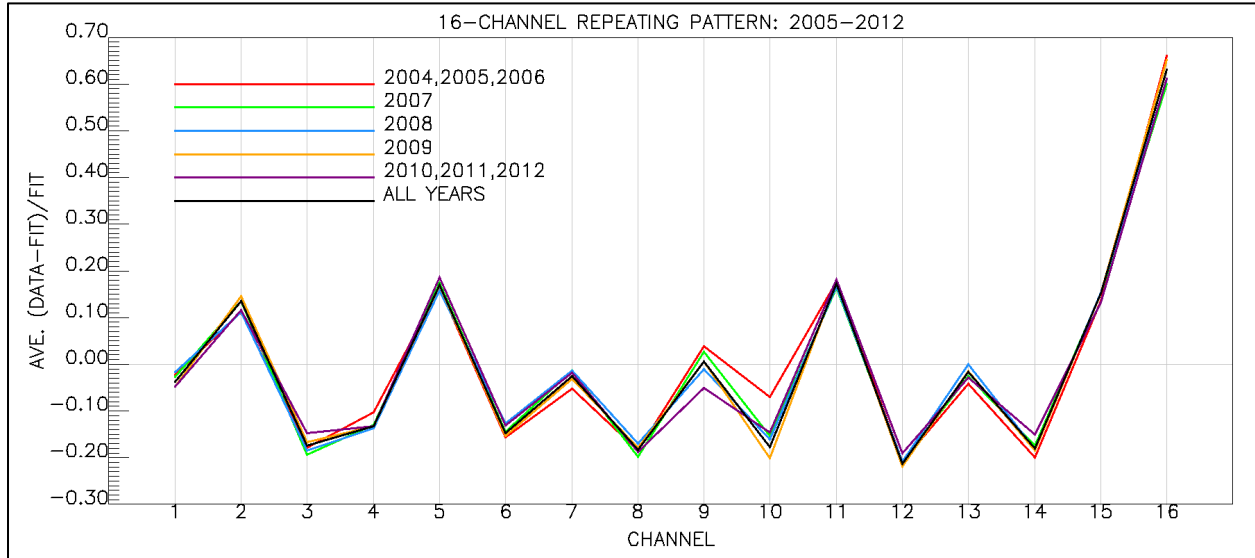

Figure 7. The repeating pattern extracted from LEF spectra summed over six different periods between 2004 and 2012, as seen in the legend. The pattern is expressed as a relative difference between the data and a linear fit to the data. Variation in the pattern is shown to be minimal over the duration of the mission.

6. Background Subtraction

Background subtraction involves fitting a model function to an appropriate subset of "background" ion counts. In many cases a flat background or a piecewise flat background can be used to approximate the true background, as was done in Figures 5 and 12, for example. However, a slightly more complex model function can account for the exponential shape of the background overlapping the ST hydrogen peaks below channel 350 as well as the non-zero slope of the linear parts of the ST and LEF backgrounds above channel 350.

To determine an appropriate background model for the TOF data, ST spectra were first summed over the same altitude, energy, and time ranges as the corresponding LEF spectra in Figure 6 in order to obtain well-resolved ST background spectra. Three of these five summed ST spectra are shown in Figure 8. The repeating pattern corrections extracted from the summed LEF spectra were then applied to the corresponding summed ST spectra to reduce the RPN. Finally, a model function of the form

$$(7) \qquad f_{BG}(x) = a_0 + a_1 x + a_2 e^{-a_3(x-a_4)}$$

was found to adequately capture the behavior of the RPN-reduced background for the summed spectra. Note that for LEF spectra acquired within ~23 Rs of Saturn, the a_2 parameter in Eq. 7 can be set to zero yielding a purely linear background model because the low TOF channels containing the exponential background component are not sampled. Moreover, the exponential component of the background should be reduced or absent for LEF spectra because the electric field in the TOF chamber drives penetrating and secondary electrons away from the LEF detector and onto the ST detector.

Constraints	Initial Guess
$0 \leq a_0 \leq y_{max}$	$a_0 = 0$
$-\infty \leq a_1 \leq 0$	$a_1 = 0$
$0 \leq a_2 \leq 2\, y_{max}$	$a_2 = y_{max}$
$0.001 \leq a_3 \leq 1$	$a_3 = 0.03$
$0 \leq a_4 \leq 200$	$a_4 = 0$

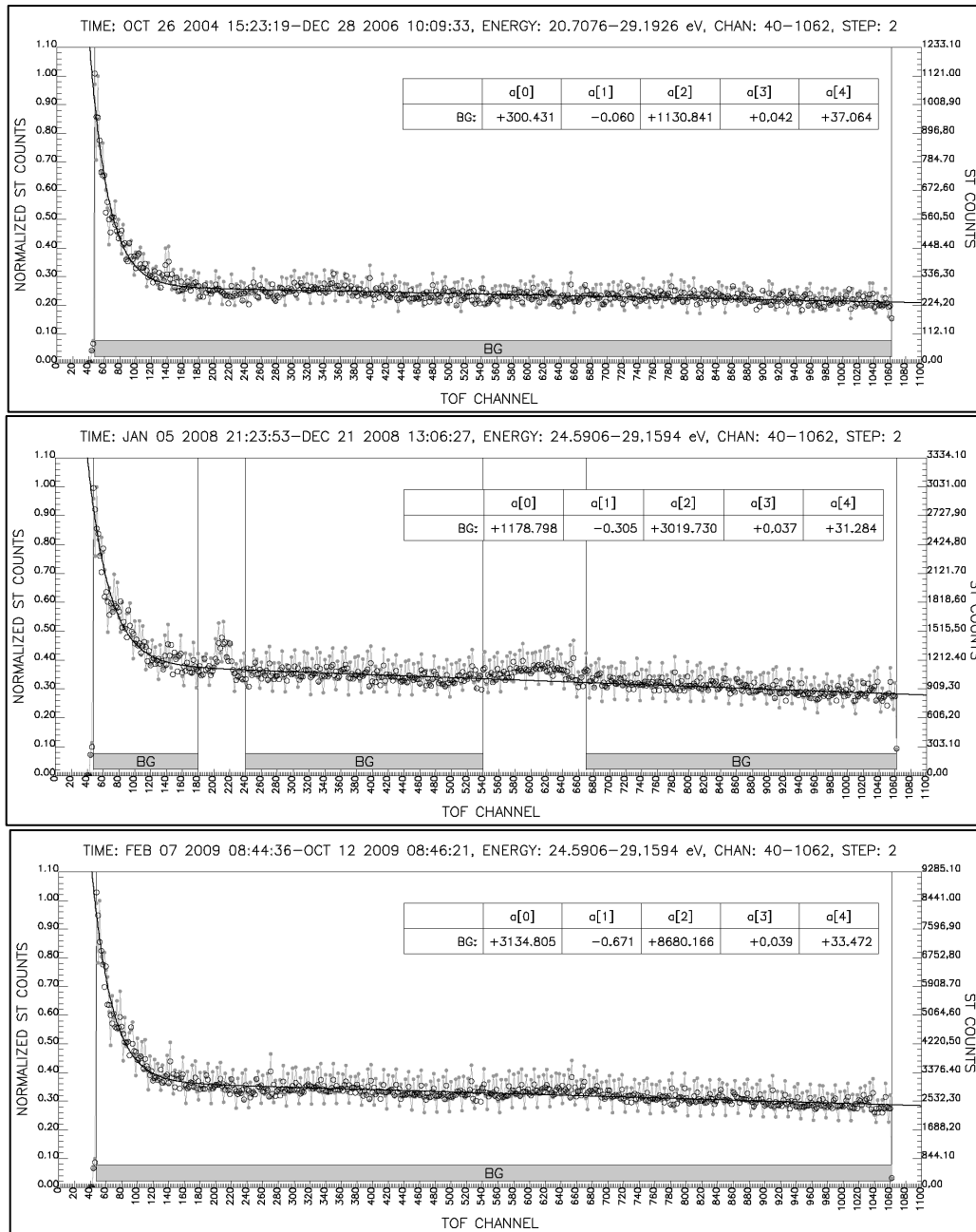**Table 4. Parameter constraints used for background model fitting with Eq. 5.**

Figure 8. Characterization of background model using summed ST spectra. The model fits are indicated by solid black lines and fit parameters are tabulated in the insets. Filled gray circles represent the summed raw data and open black circles represent the pattern-corrected data.

The fits to the RPN-reduced ST spectra were performed with mpcurvefit.pro. Table 4 lists the parameter constraints and initial guesses that were provided as input to mpcurvefit.pro. In the table, y_{max} represents the maximum count for a given spectrum. In Figure 8 the maximum count aligns with 1 on the normalized y-axis and the points selected as background for fitting are those points falling within any of the selected background intervals, which are indicated by gray bands labeled "BG" just above the x-axis. Filled gray circles represent the summed raw data and open black circles represent the RPN-corrected data. Solid black lines in Figure 8 illustrate the best-fit background curves with the associated fit parameter values tabulated in the insets. Intervals containing obvious peaks were omitted from the background fits.

The background model validated in the above fits can be applied to either summed or individual ST and LEF spectra. Figure 9 illustrates a background fit for a single B-cycle from the T40 Titan encounter. Recalling that ST peak positions vary considerably with energy above ~200 eV, the data have been summed over the first 15 collapsed energy steps (between 1.3 eV and 234.6 eV) sampled during this period. In this example, several TOF intervals labeled "BG" along the x-axis can be identified as "background-only" intervals with relative certainty. These intervals can therefore be defined by their left and right limits alone. The 16-channel pattern correction has not been applied to this spectrum because, while the count accumulation is sufficient to distinguish the background, it is likely still insufficient to ensure that the correction does not introduce spurious counts.

Figure 9. Example of a background fit for a relatively low-count spectrum from the T40 Titan encounter, in which "background-only" intervals can be selected for fitting.

This background model can be used on very low-count spectra as well. However, for very low-count spectra it can be difficult to identify background-only intervals for fitting. In these cases it may be useful to produce a spectrum histogram and separate background counts from peak counts based on histogram shape–the logic being that background counts comprise the bulk of the distribution while peak counts populate the tail. In Figure 10, for example, the right-hand panel shows a normalized histogram where bar length (here plotted along the x-axis) indicates the number of counts greater than or equal to the lower edge of the associated bar.

The left-hand "BG" interval in Figure 10 bounds a fairly well-resolved portion of the low-channel exponential background that does not appear to overlap with any peaks. For the rest of the spectrum it is less clear where the background ends and the peaks begin. The histogram half-width at half-max falls at ~ 0.1875 on the normalized (left) y-axis, suggesting that the majority of points below this value comprise background and the majority above comprise peaks. The right-hand "BG" interval in Figure 11, extending from channel 100 to channel 1062, has therefore been given a normalized upper bound of 0.1875 such that points above this value are excluded from the interval. The resulting background points are indicated by thick black circles, while the solid black line indicates the best fit of $f_{BG}(x)$ (Eq. 5) to this subset of points. The associated fit parameters are tabulated in the inset.

Figure 10. Example of a background fit for a very low-count spectrum from the T40 Titan encounter, in which a histogram of the number of counts greater than or equal to the lower edge of each bar is used to select a subset of points for background fitting.

7. Calibration

After a TOF spectrum has been reconstructed, RPN-reduced, and background subtracted, it can be analyzed to extract peak shapes for particular molecular ion species. This analysis is based on IMS calibrations using a broad range of incident ion species and energies. A limited amount of pre-flight data was taken at Los Alamos National Laboratory using the flight unit before it was integrated with the flight TOF electronics and the entire CAPS instrument calibrated at Southwest Research Institute. Following launch a second unit based on the IMS prototype was upgraded to match the characteristics of the original flight unit as closely as possible and then calibrated at Goddard Space Flight Center (GSFC). Tables 5 and 6 show the ion species and energies used in calibration, and Appendix A provides a detailed description of the calibration facilities and procedures.

Amu/Charge	Energy (eV)	# of Experiments	Amu/Charge	Energy (eV)	# of Experiments	Amu/Charge	Energy (eV)	# of Experiments
1	16440	1	14	19490	1	18	9740	1
12	1024	1	14	21330	1	18	27560	1
12	1024	2	14	23170	1	19	4096	1
12	4096	1	14	25370	1	19	9740	1
12	9740	1	14	27560	9	19	27560	1
12	16390	1	14	27560	1	20	1024	1
12	27600	1	14	27560	1	20	4096	1
13	1024	1	14	27560	2	20	9740	4
13	9740	1	15	1000	1	20	9740	2
13	11590	1	15	1024	1	20	9740	1
13	13770	1	15	9740	1	20	9740	3
13	15080	1	15	9740	1	20	13770	1
13	16390	1	15	9740	2	20	16390	4
13	17940	1	15	27560	1	21	1000	2
13	19490	1	16	1024	2	21	1024	4
13	21330	1	16	1024	1	21	4096	1
13	23170	1	16	1024	1	21	4097	2
13	27560	1	16	2050	1	21	6890	1
14	512	1	16	2900	1	21	9740	6
14	1024	1	16	4097	1	21	11590	1
14	1024	4	16	4870	1	21	11590	1
14	1024	1	16	5790	1	21	13770	1
14	1024	1	16	6890	1	21	15080	1
14	1024	1	16	8190	1	21	16390	1
14	2050	1	16	9740	1	21	17940	1
14	2900	1	16	9740	1	21	19490	1
14	4096	3	16	11590	1	24	11590	1
14	4097	1	16	13770	1	28	1000	1
14	4100	2	16	15080	1	28	1024	5
14	4870	1	16	16390	1	28	9740	3
14	5790	1	16	16440	2	28	9740	4
14	6890	1	16	17940	1	28	11590	1
14	8190	1	16	19490	1	28	16390	4
14	9740	1	16	19490	1	32	11590	1
14	9740	1	16	21330	1	40	1000	1
14	9740	6	16	23170	1	40	1024	1
14	9740	1	16	25370	1	40	4097	3
14	11590	1	16	27560	1	40	9740	1
14	13770	1	16	27560	1	40	9740	1
14	15080	1	17	1024	1	40	9740	1
14	16390	1	17	9740	1	40	13710	1
14	16440	30	17	27560	1	40	13770	1
14	17940	1	18	1024	1	40	16390	1
14	19490	1	18	4096	2	40	27560	1

Table 5. Calibration species and energies taken pre-flight with the IMS/CAPS Flight Unit at Southwest Research Institute.

Ion Species	Energy (eV)	Ion Species	Energy (eV)	Ion Species	Energy (eV)	Ion Species	Energy (eV)
20Ne	64	C2H6	1024	H	1024	N	1024
20Ne	125	C2H6	2000	H	1024	N	1024
20Ne	250	C2H6	3500	H	5000	N	1024
20Ne	375	C2H6	5000	H	10000	N	1024
22Ne	20	C2H6	10000	H	15000	N	1024
22Ne	64	C2H6	15000	H2	64	N	1024
22Ne	64	CH4	64	H2	120	N	1024
22Ne	125	CH4	125	H2	250	N	1024
22Ne	375	CH4	250	H2	375	N	1024
Ar	64	CH4	375	H2	500	N	4097
Ar	125	CH4	500	H2	1024	N	5000
Ar	250	CH4	1024	H2	2000	N	9740
Ar	375	CH4	2000	H2	3500	N	10000
Ar	500	CH4	3500	H2	5000	N	15000
Ar	1024	CH4	5000	H2	10000	N	16400
Ar	5000	CH4	10000	H2	15000	N2	64
Ar	10000	CH4	15000	H2O	64	N2	125
Ar	15000	CO	64	H2O	125	N2	250
C	64	CO	125	H2O	250	N2	375
C	125	CO	250	H2O	375	N2	500
C	250	CO	375	H2O	500	N2	1024
C	375	CO	500	H2O	1024	N2	2000
C	500	CO	1024	H2O	2000	N2	2000
C	1024	CO	2000	H2O	3500	N2	3500
C	5000	CO	3500	H2O	5000	N2	3500
C	10000	CO	5000	H2O	10000	N2	5000
C	15000	CO	10000	H2O	15000	N2	10000
C2H2	64	CO	15000	He	64	N2	15000
C2H2	125	CO2	64	He	125	Ne	500
C2H2	250	CO2	125	He	250	Ne	1024
C2H2	375	CO2	250	He	375	Ne	5000
C2H2	500	CO2	375	He	500	Ne	10000
C2H2	1024	CO2	500	He	500	Ne	15000
C2H2	2000	CO2	500	He	1024	O	64
C2H2	3500	CO2	1024	He	1024	O	125
C2H2	5000	CO2	1024	He	1024	O	250
C2H2	10000	CO2	2000	He	5000	O	375
C2H2	15000	CO2	3500	He	10000	O	500
C2H4	64	CO2	5000	He	15000	O	500
C2H4	125	CO2	5000	N	64	O	1024
C2H4	250	CO2	10000	N	125	O	5000
C2H4	375	CO2	15000	N	250	O	10000
C2H4	500	H	64	N	375	O	15000
C2H4	1024	H	120	N	500	O2	64
C2H4	2000	H	250	N	500	O2	125
C2H4	3500	H	375	N	500	O2	250
C2H4	5000	H	500	N	500	O2	375
C2H4	10000	H	1024	N	500	O2	500
C2H4	15000	H	1024	N	500	O2	1024
C2H6	64	H	1024	N	500	O2	2000
C2H6	125	H	1024	N	500	O2	3500
C2H6	250	H	1024	N	1024	O2	5000
C2H6	375	H	1024	N	1024	O2	10000
C2H6	500	H	1024	N	1024	O2	15000

Table 6. Calibration species and energies taken pre-flight with the IMS Prototype Unit at GSFC

Figure 11 shows examples of TOF calibration data using a mono-energetic beam of water molecules (H_2O^+). The largest peak in the ST spectrum (top panel) corresponds to neutral O fragments from the water molecules, while the second largest peak corresponds to O^- fragments and the small peak near channel 200 comprises neutral H fragments. In the LEF spectrum (bottom panel) the far right peak represents O^+ fragments while the left peak represents H^+ fragments. Note that the LEF and ST hydrogen peaks have roughly the same magnitude, but the magnitude of the LEF oxygen peak is roughly 100 times less than that of the ST oxygen peaks. This is an effect of the atomic physics of foil collisions, which results in a relatively small number of positively charged fragments leaving the foil as compared to the number of neutral and negative fragments. Note also that the calibration peaks tend to be narrower than those observed in flight data (calibration was performed with mono-energetic ions and a fixed beam angle with respect to the instrument aperture). Similarly, peaks acquired during flybys under ram conditions tend to be narrower than peaks acquired in hot plasma environments.

8. Spectrum Deconvolution

After RPN reduction and background subtraction, determining the relative amounts of different ion fragments represented in a given spectrum is best accomplished by fitting an asymmetric peak model for each fragment. Figure 11 illustrate this peak asymmetry. ST peak positions tend toward lower TOF with increasing energy while LEF peaks tend toward higher TOF with increasing energy, and ST peak tails stretch toward higher TOF while LEF peak tails stretch toward lower TOF. The details of these dynamics can be found in Young et al. 2007. In short, neutral and negative ion fragments exit a carbon foil and travel "straight through" to the ST detector in the linear electric field so that their times of flight generally decrease with increasing energy and velocity. Positive fragments with energies less than 16 keV, on the other hand, are reflected in the electric field after traveling some distance toward the ST detector. The higher their mass/charge the deeper they penetrate before turning around, and so their times of flight generally increase with mass/charge. Those positive fragments with energies above 16 keV are able to reach the ST detector, decelerating along the way, and so contribute to the respective ST peak tail. In reality ion fragments exit the carbons foils with a range of angles due to intra-foil collisions, and with a range of energies due to ESA energy acceptance and collisional energy loss within the foils. The energy acceptance and angular distribution primarily determine peak width, while collisional energy loss within the foil lengthens the TOF to the ST detector (rightward tail) and shortens the TOF to the LEF detector (leftward tail) as discussed above. Note that LEF peaks are narrower and their asymmetry less pronounced because positive ions are time-focused by the linear electric field.

The Logistic Power Peak (LPP) function was determined during calibration to best represent the shapes of the TOF peaks. The LPP function takes the following form:

(8) $$f(x) = \frac{a_0}{a_3}\left[1 + e^{\left(\frac{x + a_2 * \ln(a_3) - a_1}{a_2}\right)}\right]^{\frac{-a_3 - 1}{a_3}}\left[e^{\left(\frac{x + a_2 * \ln(a_3) - a_1}{a_2}\right)}\right](a_3 + 1)^{\frac{a_3 + 1}{a_3}}$$
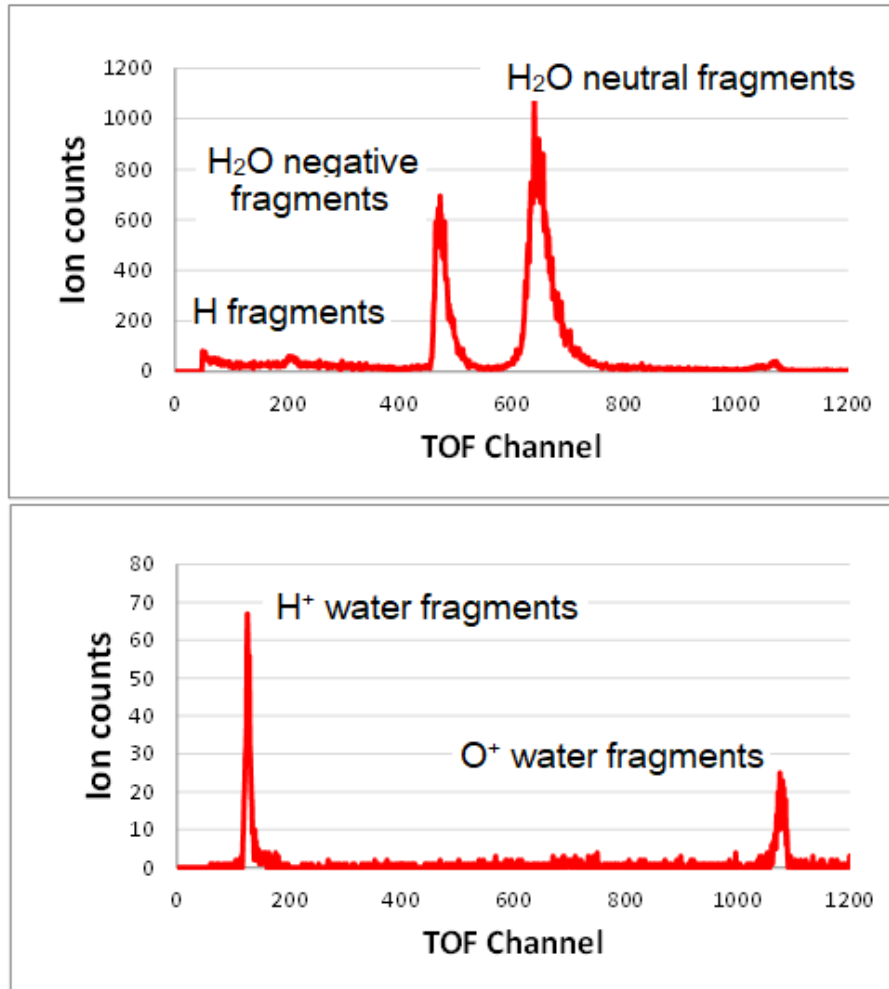
Figure 11. 500 eV ST water ion spectrum (top) and 500 eV LEF water ion spectrum (bottom) from post-launch calibration measurements.

where x is the TOF channel. The function parameters are a_0 (peak amplitude), a_1 (peak position), a_2 (peak width) and a_3 (peak asymmetry). Note that although the peaks are asymmetric, the peak position is defined as the position of the peak maximum (see Figure 13 below). Fitting this model to calibration peaks such as those in Figure 11 yielded expressions for a_1, a_2, and a_3 as functions of fragment species and energy. Since negative, neutral, and positive fragments travel along different trajectories from foil to detector, there are different expressions for negative, neutral, and positive fragments incident on the ST detector, and for positive fragments incident on the LEF detector. Note that the parameter calibrations assume a 2048 TOF channel scale, so the raw data must be mapped to the full set of 2048 channels prior to peak fitting as detailed in Section 3.

As stated previously, ion fragments can emerge from the carbon foil with neutral, negative, or positive charge states. Parameters for neutral fragment peaks appearing in ST spectra can be calculated using equations (9) through (11):

(9)
$$a1 = -34 + \left(18600 \sqrt{\frac{M/Q}{E}}\right) + \left(42400 \frac{M/Q}{E}\right)$$

(10)
$$a2 = 6.9 - \left(570 \sqrt{\frac{M/Q}{E}}\right) + \left(18900 \frac{M/Q}{E}\right)$$

(11)
$$a3 = 4.0 - \left(16.7 \sqrt{\frac{M/Q}{E}}\right)$$

where M is the mass of the incident molecular ion in atomic mass units (amu), Q is its charge in units of $|e^-|$, and E is its energy upon entering a carbon foil. The total energy of the molecular ion is given by

(12)
$$E = E_{incident} + 14557 \text{ eV}$$

because ions admitted through the ESA with energy $E_{incident}$ are then accelerated through an additional 14,557 eV to ensure penetration of the carbon foil. Equation (12) applies for all parameter equations (9) through (27).

Equations (9) through (11) can be used to calculate all neutral fragment peak parameters *except* for the positions of the neutral hydrogen fragment peaks. If the incident molecular ion is simply H^+, then the position of the associated H peak is given by:

(13)
$$a1 = \left(43400 \frac{M/Q}{E}\right) + \left(17400 \sqrt{\frac{M/Q}{E}}\right) + 2.$$

Similarly, if the incident molecular ion is H_2^+, then the position of the associated H fragment peak is given by:

(14)
$$a1 = \left(43400 \frac{M/Q}{E}\right) + \left(17400 \sqrt{\frac{M/Q}{E}}\right) + 10.$$

The parameters for negative hydrogen fragment peaks are given by:

(15)
$$a1 = 472 + \left(179 \log \sqrt{\frac{M/Q}{E}}\right)$$

$$(16) \qquad a2 = 6.0 - \left(575 \sqrt{\frac{M/Q}{E}} \right) + \left(20700 * \frac{M/Q}{E} \right)$$

$$(17) \qquad a3 = 4.0 - \left(16.7 \sqrt{\frac{M/Q}{E}} \right)$$

where equation (15) is valid for $a3 \geq 1$.

Likewise, the parameters for negative carbon fragment peaks are given by:

$$(18) \qquad a1 = 1366 + \left(628 \log \sqrt{\frac{M/Q}{E}} \right)$$

$$(19) \qquad a2 = -5.6 + \left(522 \sqrt{\frac{M/Q}{E}} \right) - \left(757 \frac{M/Q}{E} \right)$$

$$(20) \qquad a3 = 4.5 - \left(35.8 \sqrt{\frac{M/Q}{E}} \right)$$

where equation (18) is valid for $a3 \geq 1$.

Lastly, the parameters for negative oxygen fragment peaks are given by:

$$(21) \qquad a1 = 1544 + \left(729 \log \sqrt{\frac{M/Q}{E}} \right)$$

$$(22) \qquad a2 = -4.4 + \left(453 \sqrt{\frac{M/Q}{E}} \right) - \left(5300 \frac{M/Q}{E} \right)$$

$$(23) \qquad a3 = 2.2 + \left(45.8 \sqrt{\frac{M/Q}{E}} \right)$$

where equation (21) is valid for $a3 \geq 1$.

Spectral analysis is carried out by selecting an appropriate set of representative LPP peaks for a given spectrum and fitting the sum of peaks to the data. In general any subset of LPP peak parameters can be optimized by the fitting algorithm of choice, but the most straightforward method is to use equations (9) through (23) to fix all but the peak amplitudes and allow the algorithm to find the best-fit peak amplitudes. Once all peak parameters are known the relative amount of a particular molecular ion species is given by the ratio of the area under its peak to the combined area under all peaks in the spectrum. Figure 12 shows the best-fit results for deconvolution of a complex in-flight ST spectrum.
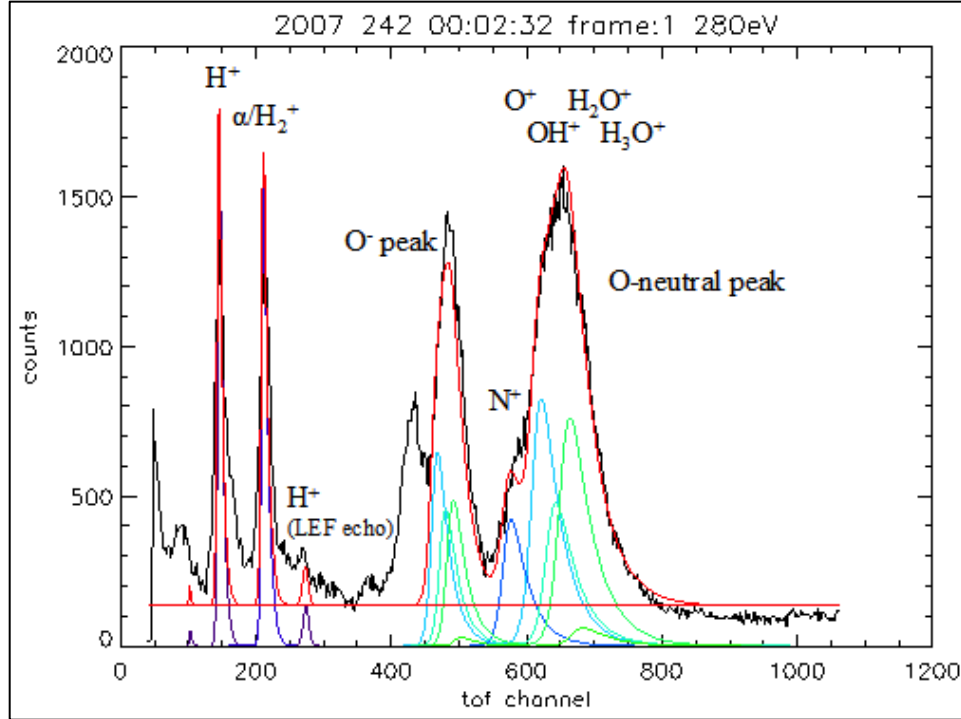

Figure 12. Best-fit sum of LPP peaks for ST data observed on 2007 DOY 242.

The black trace in Figure 12 represents the TOF data, while the colored curves are least-square fits using the LPP model functions. The sum of all model peaks is given by the red line. Note that there are two broad water ion (W^+) peaks centered near channels 475 and 675. The right peak is produced by neutral oxygen fragments from W^+ molecular ions and the left by negative oxygen fragments from W^+ ions. The small peak sitting on the left shoulder of the O^- peak is produced when an H^- ion fragment starts the TOF clock instead of an electron and so it is not included in the fit. Also note that the fit in Figure 12 assumes a flat background level instead of the linear + exponential background model described in Section 6.

LEF spectral fitting follows the same process used for ST fitting. LPP parameters for all positive molecular ion fragment peaks are given by the following equations:

(24) $\qquad a1 = 278\sqrt{M_f} - 201\sqrt{M_f}\,e^{-0.00029\,E_f}$

$$(25) \qquad a2 = 2.3 - \left(190 \sqrt{\frac{M/Q}{E}} \right) + \left(380 \, \frac{M/Q}{E} \right)$$

$$(26) \qquad a3 = -1.8 + \left(150 \sqrt{\frac{M/Q}{E}} \right)$$

where M_f is the fragment mass (in amu) and E_f is the mass-weighted fragment energy given by

$$(27) \qquad E_f = \frac{M_f}{M} \, E.$$

Figure 13 shows the result of applying the model fits to the background corrected LEF data originally shown in Figure 5 above.
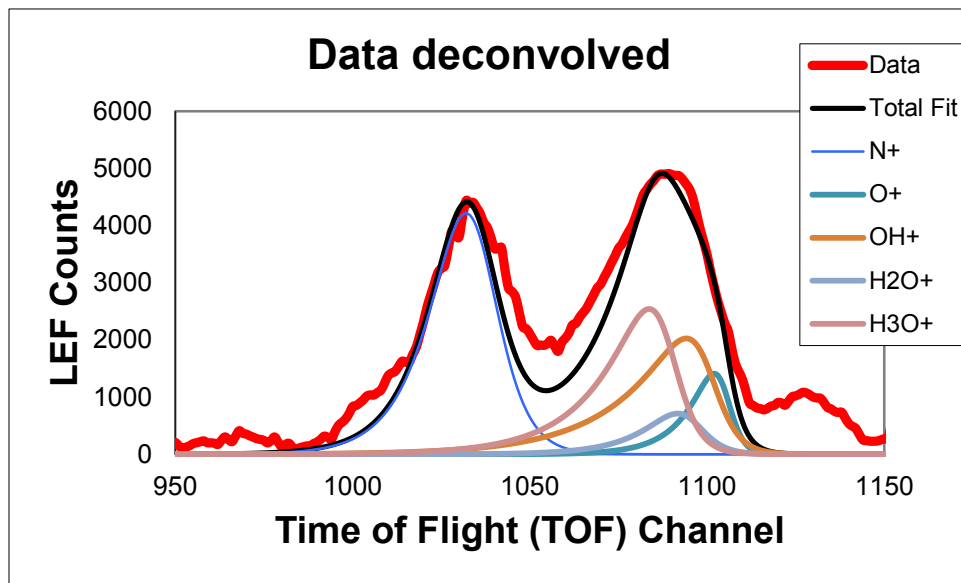

Figure 13. Best-fit sum of LPP peaks for the LEF data corresponding to the ST data in Figure 5.

After Cassini arrived at Saturn and TOF observations began, it became apparent that in-flight peaks are somewhat wider than those recorded during laboratory calibration. Figure 14 shows examples of peak width discrepancies in ST and LEF spectra (compare with the water spectra in Figure 11). Post-launch numerical modeling as well as laboratory measurements and flight-data analysis have been conducted to investigate the differences between calibration and in-flight peak profiles for W^+ ions and the results of those studies can be summarized in the following recommendations:

1) W^+ fragment peak position (the $a1$ parameter) should be shifted by 8 TOF channels toward longer TOF,

2) W⁺ fragment peak width (the $a2$ parameter) should be multiplied by a factor of 1.4,

3) W⁺ fragment peak asymmetry (the $a3$ parameter) should be multiplied by a factor of 1.1.

At this point in time, it appears that the flight data is responding as if the carbon foils became thicker than originally determined. However, it is not currently clear what is causing this phenomenon. Therefore, users should be wary when applying the above correction factors since the constituent W⁺ peaks are closely spaced along the TOF spectrum. Shifting and widening the peaks may increase their overlap and further complicate deconvolution.
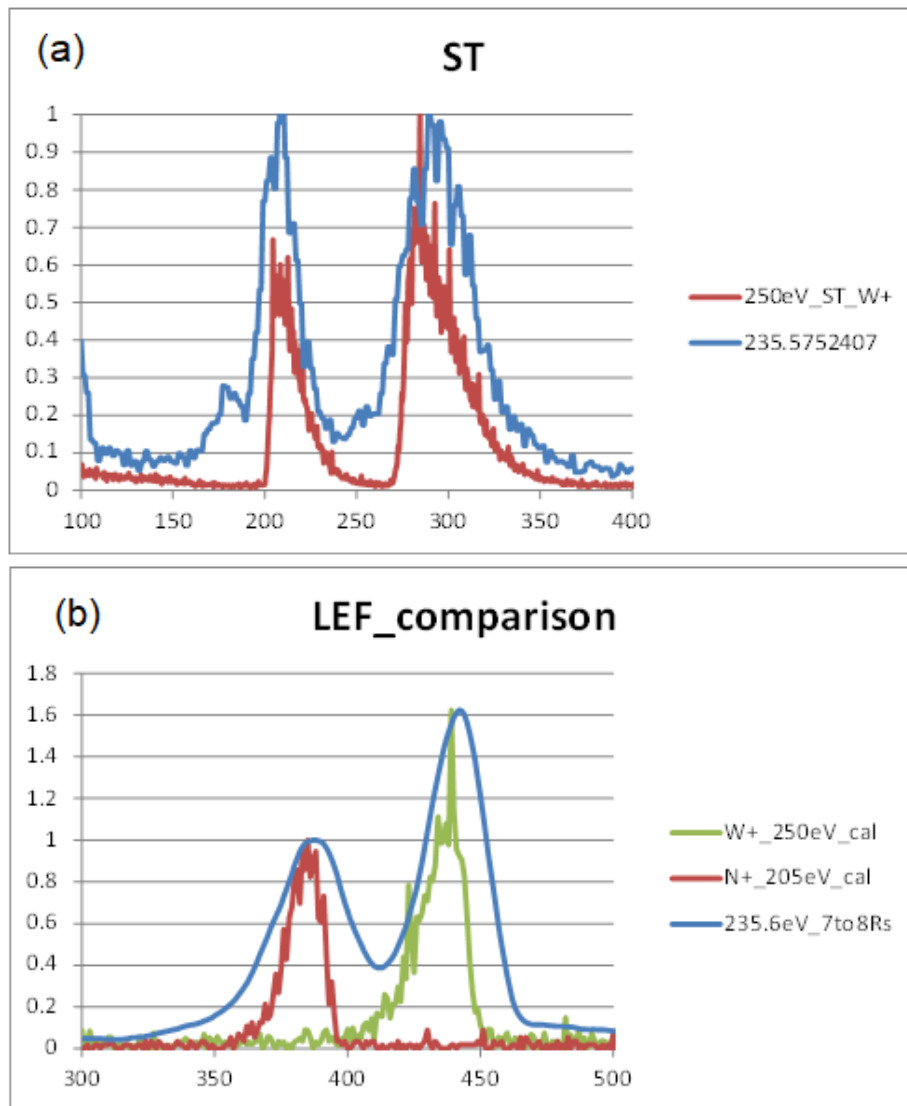

Figure 14. Comparison of 250 eV ST calibration peak widths (a) and comparison of 250 eV LEF calibration peak widths (b) to those observed in flight. Flight data is represented by a blue line in each plot, and calibration data is represented by red and green lines.

9. Ghost Peaks

Users must be careful to avoid identifying "ghost" peaks in the ST spectra as legitimate ion peaks. In general, ghost peaks occur when stray ion fragments strike surfaces other than the detector active areas, generating secondary electrons that accelerate toward the ST detector and generate false stop events. If a particular stray trajectory occurs frequently enough, the associated false stops will accumulate and produce a ghost peak. These ghost peaks can occur in TOF ranges devoid of other peaks, or they can overlap with legitimate peaks. A common type of ghost peak is an LEF echo, for which a positive ion en route to the LEF detector instead strikes the LEF suppression grid or grid holder and ejects an electron than reaches the ST detector almost instantaneously relative to the parent fragment's TOF. In the case of an LEF echo the resulting ghost peak can be found in the ST spectrum at the location that its parent fragment peak would occupy in the LEF spectrum.
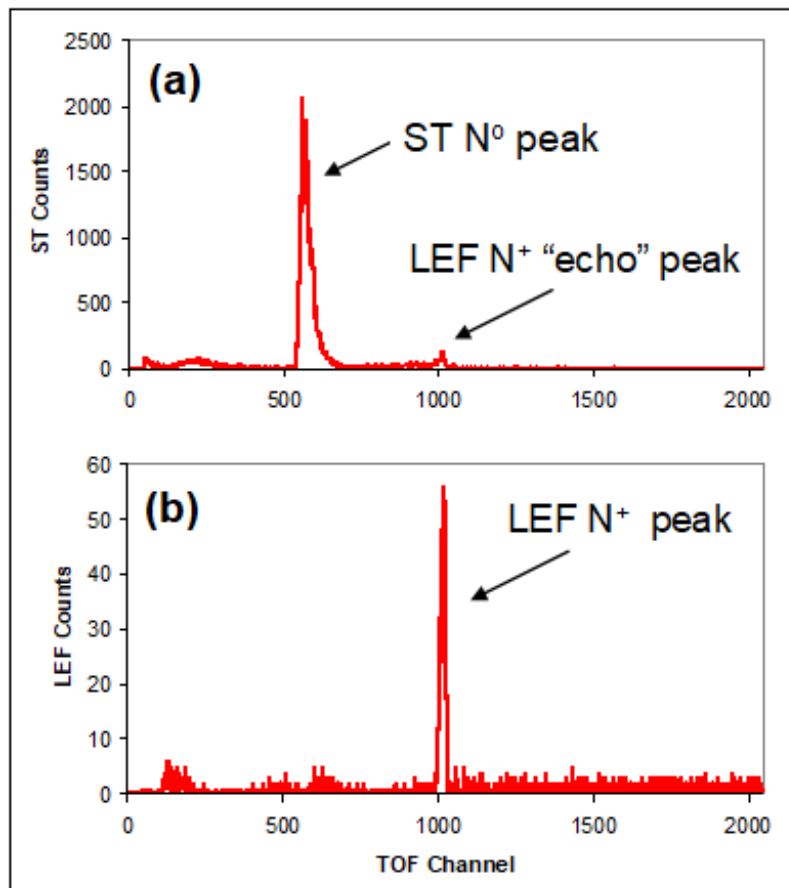

Figure 15. ST and LEF spectra for N^+ taken from calibration data.

While ghost peaks should not be misidentified as true peaks prodced by ion fragments, they may be used to qualitatively verify some details of ion composition. For example, O^+ and CH_4^+ produce overlapping ST peaks. However, the C^+ fragment yield from the carbon foil is very low, while the O^+ fragment yield is high. As a result, O^+ produces a prominent LEF echo while CH_4^+

does not. Figure 15 shows an example of an echo peak taken from calibration data (Figure 12 shows echo peaks that are embedded in a much more complex flight spectrum). Figure 15a shows an ST spectrum with a neutral nitrogen peak centered near channel 520 and an associated smaller echo peak centered near channel 1000, which is the location of the N^+ peak in the LEF spectrum. Although the scales in the two plots are very different, note that the amplitude of the nitrogen echo peak is about 2.5 times that of the LEF peak (135 vs. 55). Thus when searching for species in the data, LEF spectra should be consulted to identify echo peaks in the ST spectra that may verify their presence, bearing in mind that an echo may be larger than the corresponding LEF peak.

There are other ways for ghost peaks to be generated in the ST spectra. Scattered ions and ion fragments may accidently impact other surfaces inside the optics and eventually they, or secondary electrons they generate, may reach the ST detector. These ghosts tend to be very diffuse and simply add to the broad background discussed earlier or can be identified in relatively "empty" spectra and be removed.

10. Calculating Phase Space Density from TOF Spectra

Once a spectrum has been deconvolved and counts partitioned according to species as outlined above, those counts must be converted to phase space density (PSD) in order to extract physical quantities (i.e. moments of the distribution) such as density and temperature. Methods for PSD and moment calculation using IMS data can be found in

> Thomsen et al. (2010), Survey of ion plasma parameters in Saturn's magnetosphere, *J. Geophys. Res., 115*, A10220, doi:10.1029/2010JA015267.

and also in

> Thomsen, M. F., and D. M. Delapp (2005), Numerical moments computation for CAPS/IMS, Los Alamos National Laboratory Report LA-UR-05-1542.

which can be downloaded at

> http://nis-www.lanl.gov/nis-projects/caps/Moments_Computation.pdf.

While the higher $\Delta M/M$ of the LEF data provides useful composition information for deconvolving ST spectra, it is recommended that only ST data be used for moment calculation because the higher efficiency of the ST detector yields better-resolved spectra and, therefore, more accurate moments. For a given ion species in the plasma environment the PSD satisfies the relationship

(28) $$\frac{C(s,E)}{\tau} = G(E)\,\varepsilon(s,E)\,f(s,E)\,v(s,E)^4$$

where $C(s, E)$ is the number of counts measured for ions of species s with energy E in a time τ, $G(E)$ is the energy-dependent geometric factor of the IMS tophat including entrance apertures and ESA, $\varepsilon(s, E)$ is the probability that coincident start and stop events are detected for ions of species s with energy E that make it through the ESA, $f(s, E)$ is the PSD to be determined, and

$$(29) \qquad v(s, E) = \sqrt{\frac{2E}{M_s}}$$

is the ion speed for species s with mass M_s and energy E. Note that the PSD obtained from equation (28) must be interpreted either as a partial PSD or a partial integration over a PSD. Since the TOF integration period is relatively long ($\tau \approx 256, 512,$ or 1024 s) the actuated IMS FOV can sweep out nearly a full hemisphere during a single integration period; or if actuation is restricted it may sweep over the same direction twice during a single integration period. In any case, the full sky is never viewed during a single B-cycle. Thus PSD's derived from TOF data provide very low velocity space resolution and incomplete velocity space coverage. Fortunately, many lower-energy ions tend to move in a co-rotational direction. So if the instrument field of view completely encompasses the plasma co-rotational direction, this method can provide a reasonable approximation of the PSD. These issues are discussed in Thomsen et al., 2010 and in Section 10.4 of Wilson et al.

The geometric factor, $G(E)$, and detection efficiency, $\varepsilon(s, E)$, were obtained by combining laboratory measurements with extensive instrument simulations. The TOF geometric factor is given by the expression

$$(30) \qquad G(E) = 0.00427 + 0.00169 \left(\frac{E}{1000}\right)^{-0.1379} \text{cm}^2 \text{ sr eV/eV}$$

where E is the energy of the incident molecular ion in eV *prior* to post-ESA acceleration. Note that the geometric factor in equation (30) is a sum over the geometric factors of the 8 ST anodes. However, due to instrument symmetry the geometric factor is the same for each anode, and so the expression in equation (30) is simply 8 times the geometric factor of a single anode.

While there is a convenient expression for SNG efficiencies (see Wilson et al.), no such expression presently exists for TOF efficiencies. Instead, TOF efficiencies for a variety of ion species and ion energies are tabulated in 4 different files available on the PDS. These files are listed in Table 7. Note that although they are related, the SNG and TOF efficiencies are *not* interchangeable because the TOF efficiencies encode the probability of *coincident* start and stop events while the expression for SNG efficiency encodes only the start probability. Users should exercise caution if interpolating or extrapolating the tabulated values to ion species and energies that are not represented in the efficiency files. See, for example, Section 6 in

> Woodson et al. (2015), Ion composition in Titan's exosphere via the Cassini Plasma Spectrometer I: T40 encounter, *J. Geophys. Res. Space. Physics*, *120*, 212–234, doi:10:1002/2014JA020499

for examples of TOF efficiency interpolation/extrapolation and application. It is also important to remember that a given TOF spectrum may be integrated over 2 ESA energy levels, and that each ESA energy level has a pass band of $\pm 8.5\%$ ($\Delta E/E = 17\%$). Therefore a range of efficiency values will apply when using a deconvolved TOF peak to calculate the partial PSD for the associated ion species.

The discussion above involves calculating the partial PSD using only IMS TOF data. However, it is also possible to calculate the PSD by partitioning IMS SNG counts according to the relative abundances determined from the associated TOF spectra, as discussed in Thomsen and Delapp (2005) and Thomsen et al. (2010). Recall that SNG counts record all start events whereas TOF counts record only coincident start and stop events, and so SNG spectra typically have much better count accumulation than TOF spectra. SNG counts are also integrated over much shorter 32-second A-cycles and binned into 8 sectors according to incident ion trajectory, yielding more information about the velocity space distribution of the ambient plasma. If this method is used, relative TOF abundances should be extracted as described in Section 8 above but calculation of the PSD requires a different geometric factor, detection efficiency, and measurement time τ than are used in equation (28). Note also that since TOF counts are integrated over all 8 ST anodes and over all constituent A-cycles, partitioning SNG counts according to TOF relative abundances assumes, perhaps incorrectly, that the plasma composition does not change from sector to sector or from A-cycle to A-cycle.

Detection Efficiency	Source File
LEF	tot_eff_full_lef.txt
ST total efficiency summed over all TOF channels including ghost peaks	tot_eff_full_st.txt
ST "neutral" efficiency summed over all TOF channels comprising neutral peaks	neu_eff_full_st.txt
ST "neutral-negative" summed over all TOF channels comprising neutral and negative peaks combined	neu_neg_eff_full_st.txt

Table 7. Files containing tabulated TOF detection efficiencies for molecular ion fragments.

Appendix A: CAPS IMS Calibration Description

1. Introduction

The calibration data taken at Southwest Research Institute (SwRI) prior to launch has been analyzed and used to generate expected peak position, width and asymmetry for the data being returned from Saturn. The data taken at SwRI was somewhat limited in mass (12 AMU through 40 AMU) and in energy (1024 eV to ~46 keV) but a larger amount of data was taken using both the flight unit at Los Alamos National Labs (LANL) and the prototype unit at Goddard Space Flight Center (GSFC). The additional data taken at LANL, while with the flight unit, including flight foils, was not taken at the operational high voltage of +/-14.6 kV, but rather at +/- 15 kV. And the prototype unit is a different instrument with different carbon foils, thus the behavior is not expected to be an exact duplication of the flight unit. The amount of data taken with "non-flight" like conditions is much broader than that for the flight model, ranging from 1- 44 AMU and from ~32-46.4 keV. Using this broader data set we determined the expected trends in the coefficients for the fit parameters and then used the flight calibration data to determine the coefficients themselves. Figure 1 shows a ray tracing model of nominal particle trajectories through the IMS.

Figure 1 shows earlier ion ray trace for the CAPS IMS. The red indicated incoming positive and fragments exiting the carbon foil, green indicates the start electron trajectories, blue negative ion fragments and black neutral fragments.

2. Prototype Model Calibration Data

PM Introduction: The Prototype Model (PM) calibration data was taken in two facilities at Goddard, one named Suprathermal Ion Mass Spectrometry (SIMS) Lab in Bldg. 21 (see Figure 3) which provides measurements between 64 V and 15 kV, while the other facility is in Bldg. 22 (see Figure 4) which is run by the Flight Data Systems and Radiation Effects Branch. The PM was used to repeat the flight calibration data and to get calibration data for ion species and energies not done for the Flight Model (FM).

Three methods were used to calibrate the prototype IMS TOF unit

1) The first method applied a Built in Test (BIT) mode. Pulses separated by multiples of 125ns (i.e., 125 ns, 250 ns, 375ns, 500ns, etc.) were applied to the start and stop preamplifiers.   By fitting a straight line to the data, we obtained ps/channel. The accuracy depended on the 80-MHz clock in the TDC, which was not measured at this time.

2) Second method introduced a delay cable of known length into the Start / Stop path and noted the change in the offset. The accuracy depends on the 80-MHz clock in the TDC, as well as measurement of the length of the cable.

3) The third method used the ORTEC 462 Time Calibrator to supply pulses separated by multiples of 20ns to the start and stop preamplifiers. Accuracy is specified at +/- 0.005% and is in principle factory calibrated against National Bureau of Standards WWV.

The SIMS facility, photo shown in Figure 3, which covers the energy range 64 V ≤ E/Q ≤ 15 kV has electron impact ionization sources for which various gases can be leaked into the source, ionized, extracted at nominal energy of 400 V, then passes through ISEE-3 spare Wien filter with mass resolution M/ΔM ~ 32 after which the ions can be further accelerated by a long lens system up to 15 kV. We also, have the ability to lower the potential of the ion source + WF down to 64 V or lower for low energy ion calibration measurements. The PM is a nearly identical design as the FM except for its carbon foils (CFs). The FM carbon foils nominally were ~ 0.5 μgm/cm^2 with thickness of ~ 45 Ä as reported in Young et al., 2005 (note, carbon density is usually ~ 2.253 gm/cm^2). However, estimates by Ritzau and Baragiola (1998) were ~ 75 Ä with mass density ρ ~ 1.8 gm/cm^2. Using the Goddard simulation code and the proton peak in the Saturn Orbit Insertion (SOI) outbound ST TOF data when voltage across the LEF stack = ±6 kV, the estimate carbon foil thickness was 45 Å with assumed mass density ρ = 2.253 gm/cc. The raw start/stop pulses from the PM then go into the Time to Digital Converter (TDC) designed and built by LANL and equivalent but not identical to the flight TDC. This data then goes into GSE PC also provided by LANL. The data recorded using the SIMS facility did not include the start/stop singles.
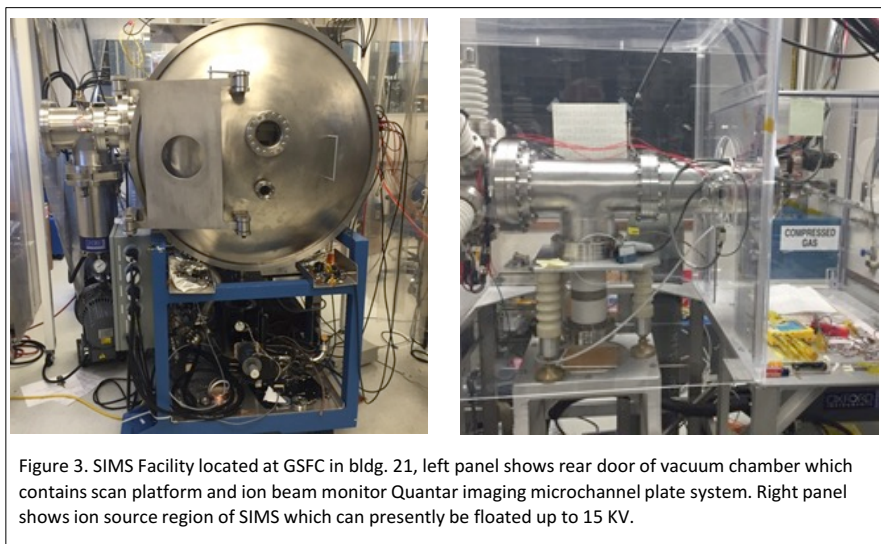

Figure 3. SIMS Facility located at GSFC in bldg. 21, left panel shows rear door of vacuum chamber which contains scan platform and ion beam monitor Quantar imaging microchannel plate system. Right panel shows ion source region of SIMS which can presently be floated up to 15 KV.

Subsequent analysis in 2006 determined that the positive voltage applied to the bottom of the LEF stack was known within 0.11%, but for the minus high voltage applied to the top of the LEF stack the precision was ~ 1%. This lower precision was due to loading effects on the voltage monitor readout when the DVM was connected to this monitor readout when at its 10 V scale, while no loading occurred when DVM at its 100 V scale. The voltage was set at 14600 V / 2000 = 7.3 V.

Figure 4 showing PM IMS in bell jar chamber that is attached to the beam line of the Medium Energy Accelerator Facility at GSFC in Bldg. 22.

The Goddard facility in Bldg. 22 is operated by the Flight Data Systems and Radiation Effects Branch, Code 561, at that facility we used their Medium Energy accelerator which can make ion measurements between 10 kV and 120 kV, for which we used measurements up to 50 kV. The setup is shown in Figure 4 which shows the IMS in bell jar chamber attached to the beam line of the accelerator. A bending magnet with series of slits was used to provide the mass analysis of the beam. The accelerator uses an electron impact ionization source and various gases can be leaked into the source. The same data acquisition system as used for the SIMS measurements was used. Again, the data was archived and analyzed by Mark Shappirio, Dennis Chornay and David Simpson.

Table 1 shows the energy and species that were measured at GSFC using the prototype unit.

Similar to the FM calibration, all data was collected as a function of TOF channel (2048) for each ion mass experiment (Table 2 in the above TOF User's Guide). The fitting spectra were then derived as four parameter Logistic Power Peak (LPP) functions for all major and minor peaks in each experiment. The fit results were put in various Excel spreadsheets and then condensed into a final spreadsheet for both ST and LEF data with each having sub-sheets with fit parameters, their uncertainties, fit quality etc. for major peak and all peaks, major and minor, stored. Using the major peaks and matching the log book indication of energy and mass, the equations to match TOF channel number to Mass and Energy were estimated. Unlike the FM

calibration, Singles data was also recorded using the facility in Bldg. 22 for energies 10 kV $\leq$ E/Q $\leq$ 50 kV.

Table 1, Energy vs. species measured during PM calibration.

Incident E	H	H2	He	C	N	O	CH4	H2O	Ne	C2H2	N2	CO	C2H4	C2H6	O2	Ar	CO2
64	X	X	X	X	X	X	X	X	X	X	X	X	X	X	X	X	X
125	X	X	X	X	X	X	X	X	X	X	X	X	X	X	X	X	X
250	X	X	X	X	X	X	X	X	X	X	X	X	X	X	X	X	X
375	X	X	X	X	X	X	X	X	X	X	X	X	X	X	X	X	X
500	X	X	X	X	X	X	X	X	X	X	X	X	X	X	X	X	X
1024	X	X	X	X	X	X	X	X	X	X	X	X	X	X	X	X	X
2000		X					X	X		X	X	X	X	X	X		X
3500		X					X	X		X	X	X	X	X	X		X
5000	X	X	X	X	X	X	X	X	X	X	X	X	X	X	X	X	X
10000	X	X	X	X	X	X	X	X	X	X	X	X	X	X	X	X	X
15000	X	X	X	X	X	X	X	X	X	X	X	X	X	X	X	X	X
16400	X	X			X	X		X	X			X		X	X	X	X
16600	X				X	X											
19500	X	X		X													
23200	X	X		X		X		X				X		X	X	X	X
27600	X	X			X			X	X			X	X		X		
32800	X	X				X		X	X			X		X		X	X
39000	X	X			X			X	X			X			X	X	X
46300	X	X		X	X	X		X	X			X		X	X	X	X

3. CAPS Ion Beam Calibration System and IMS Calibration

The Ion Beam Calibration System (IBCS) at Southwest Research Institute (SwRI) was designed and built specifically for calibration of the integrated CAPS instrument in its flight configuration (Figure 5, see Young et al., Space Sci. Rev, Vol. 114, 2005 for a detailed instrument description and a limited discussion of calibration). The three sensors comprising CAPS are the Ion Beam Spectrometer (IBS), the Electron Spectrometer (ELS), and the Ion Mass Spectrometer (IMS). In flight configuration the sensors were mounted on the Data Processing Unit (DPU) that served as mechanical platform for the three sensors. The DPU was in turn mounted on the CAPS Actuator (ACT) that formed the electrical and mechanical interfaces to the spacecraft. The ACT was clamped in flight configuration during calibration so CAPS could not rotate as it did in flight. Instead the entire instrument was mounted on a 4-axis motion system. Two translation axes were oriented perpendicular to the calibration beam, and a goniometer moved through two angles corresponding to sensor azimuth and elevation. Only IMS was fully calibrated at SwRI. Some IBS calibration took place at SwRI but most was carried out at LANL prior to delivery to SwRI. The majority of ELS calibration was performed at MSSL in the UK prior to delivery. A simple electron source was used to check ELS functionality and energy scan capability.
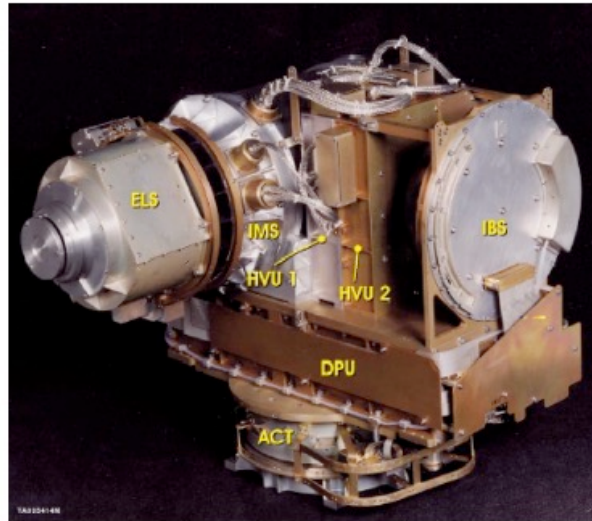
Figure 5. Photograph of CAPS Flight Model (FM) just prior to delivery to the Cassini spacecraft.
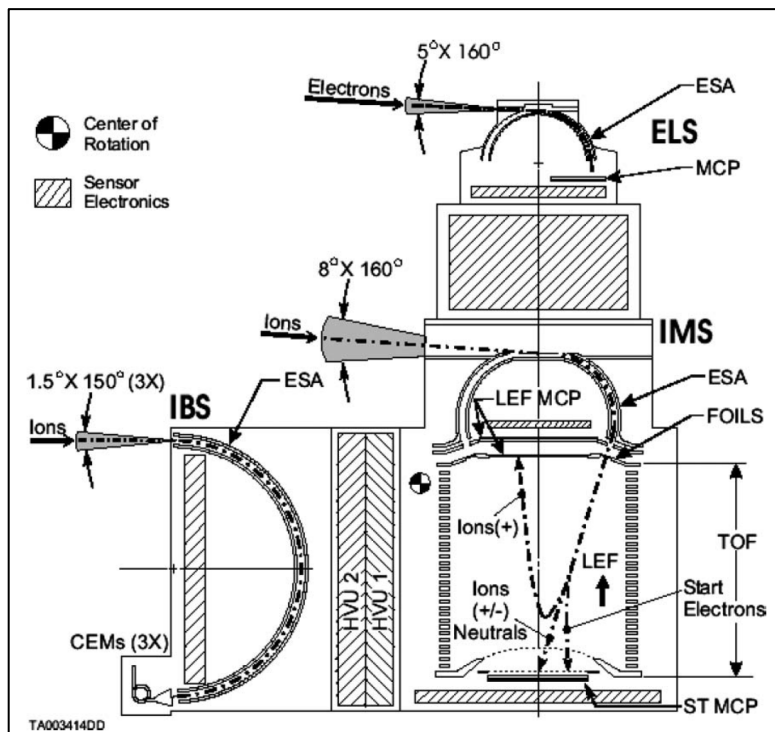

Figure 6. Cutaway schematic of the ELS, IBS and IMS optics showing their component relationships, orientations, optics, and fields-of-view (FOV).

Although the IBCS was designed primarily to calibrate IMS response as a function of energy, angle, and ion species, the system was also used to calibrate IBS and to test basic ELS functions with a simple electron source. All three sensors incorporated electrostatic energy-angle analyzers (ESAs, Figure 5), and one or more detectors. IMS had two microchannel plate detectors (MCPs), ELS had one, and IBS had three channeltron electron multipliers (CEMs). The IMS ESA was followed by a time-of-flight (TOF) mass/charge analyzer which incorporated low mass

resolution "Straight Through" (ST) optics and high-resolution "Linear Electric Field" (LEF) optics (see Young et al., 2005 for details).

4. Calibration Theory

We discuss calibration theory briefly so the considerations that went into IBCS design are understood. In general, plasma sensor calibration is based on three types of independent measurements: 1) angle and energy responses that determine the geometric factor G, 2) an efficiency factor ε that converts detector counting rate into particle flux, and 3) mass spectra in the form of a spectrum library together with deconvolution software.

The equation that relates counting rate to particle flux is:

$$C = J \, \varepsilon \, G \, \Delta t \quad \text{[counts/sample]} \tag{1}$$

where J is flux in # ions $(cm^2 \text{ sr eV/eV})^{-1}$, ε is efficiency in counts/ion, G is in cm^2 sr eV/eV, and Δt is the sampling interval. The IMS sampling interval is generally 0.0625 s but for convenience we set $\Delta t = 1$ s.

The geometric factor typically changes very little with ion energy and incident angle whereas efficiency can change significantly with energy and ion species.

Plasma parameters such as density and temperature are moments of the differential velocity distribution function f_{ij} (cf. Thomsen et al., JGR, Vol 115, A10220, 2010), where i is ion species, j is energy, and ij corresponds to mass and energy indexes used in IMS operations. The function f_{ij} has to be derived from measured counting rates as a function of energy, mass and angle of arrival:

$$f_{ij} = C_{ij} \, m_i^2 \, /\varepsilon_{ij} \, G_j \, E_j^2 \quad \text{[cm}^{-6} \text{ s}^3\text{]} \tag{2}$$

where m_i is ion mass per charge and

$$G_j = 2 \, A \, <\Delta\alpha \, \Delta E/E_j> \, \Delta\beta \; \text{[cm}^2 \text{ sr eV/eV]}. \tag{3}$$

In Eq. 3 A is the aperture area, $<\Delta\alpha \, \Delta E/E_j>$ is the coupled azimuthal angle-energy passband at energy step j, and $\Delta\beta$ is the elevation passband. The integral $<\Delta\alpha \, \Delta E/E_j>$ is obtained by scanning the $\Delta E/E$ passband at each azimuth covering $\Delta\alpha$. (Since A cannot be measured separately some authors lump ε_{ij} and A into one parameter, the effective area.)

TOF "efficiency" is dependent on many factors including the thickness and surface characteristics of the carbon foils that generate START electrons, transmission of ions through the carbon foils, efficiency of the two MCP detectors, and (strictly speaking) transmission losses from internal scattering off optical surfaces. Taking these into account then

$$\varepsilon_{ij} = T_{grids} \, T_{foils} \, T_{optics} \, \varepsilon_{foil} \, \varepsilon_{stop \, MCP} \, \varepsilon_{start \, MCP} \tag{4}$$

where T are transmission factors and ε are efficiency factors. Since these factors cannot be separated, in calibration they are lumped into a single parameter ε_{ij} which has to be calibrated

over the entire range of target ion species and energies. Table 2 shows a matrix of ion energies and species run during IMS calibration at SwRI, and post-launch calibration of the PT at GSFC.

Table 2. Calibration species and upper and lower energy limits (E1 and E2 in eV) covered during IMS FM calibrations in the IBCS at SwRI, and the IMS PT calibrations performed post-launch at GSFC.

Species	Mol. Wt.	SwRI		GSFC	
		E1	E2	E1	E2
H+	1	16440		64	15,000
H2+	2	1024	27560	64	15000
He+	4			64	15000
C+	12	1024	27560	64	15000
CH+	13	1024	27560		
CH2+	14	512	27560		
N+	14	1024	27560	64	16400
CH3+	15	1000	27560		
O+	16	1024	27560	64	15000
CH4+	16	1024	27560	64	15000
NH2+	16	1024	27560		
NH3+	17	1024	27560		
H2O+	18	1024	27560	64	15000
H3O+	19	4096	27560		
20Ne+	20	1024	16390	64	15000
21+	21	1000	19490		
22Ne+	22	1024	27560	20	375
24+	24	11590			
C2H2+	26			64	15000
C2H4+	28			64	15000
N2+	28	250	27560	64	15000
CO+	28			64	15000
C2H6+	30			64	15000
O2+	32	1000	27560	64	15000
Ar+	40	1024	16390	64	15000
CO+	40			64	15000
CO2+	44			64	15000

The third element of calibration is conversion of TOF spectra to mass/charge identifications that can be used to develop a library of TOF peaks to aid spectral deconvolution.

With reference to Figure 6, here's how the TOF system works (Young et al., 2005):
Ions going through the foils emit one or more secondary electrons that travel to the ST MCP and start the timing process (their travel time is negligible and is neglected). Ions leave the foil in positive, negative or neutral charge states. Neutrals and negative ions have a relatively straight path to the ST MCP (hence "Straight Through" terminology). Positive ions entering the Linear

Electric Field (LEF) "bounce" in the field which has the property that ions are time-focused. Hence LEF spectra are higher resolution than ST spectra which are not time focused. Positive ions above ~18 keV are energetic enough to penetrate the field and end up on the ST detector. In summary: Only positive ions with energies <17 keV end up in LEF spectra.

As an illustration of the simplest straight-through case of neutrals, the measured quantity in calibration is TOF (τ) which is converted to mass by the equation:

$$m_i \approx 2\, \tau^2\, E_{jI}\, (1 - \eta_{ij})\, (L_{ij} \cos \theta_0)^{-2} \tag{5}$$

where E_{jI} = the internal ion energy at energy step $j = (E_j + V_A)$, E_j is ion energy/charge external to the instrument, V_A is the TOF acceleration voltage (14.56 kV), η_{ij} is ion energy loss in the foil for species i at energy j, L_{ij} is the path length as a function of mass and energy, and θ_0 is the angle between the foil normal and the TOF cylinder axis (14°, see Figure 6). (Needless to say this analytical expression is for illustration purposes and has to be replaced by numerical simulations in the real world.)

There are similar, but more complex, relationships for trajectories of the other charge states and energies (Young et al., Space Sci. Rev., 2007). The quantities η_{ij} and L_{ij} cannot be measured separately so are lumped as a single parameter:

$$k_{ij} = 2\, (1 - \eta_{ij})\, (L_{ij} \cos \theta_0)^{-2} \tag{6}$$

where k_{ij} is a mass and energy dependent "constant" determined in calibration.

Mass resolution is measured by the simple conversion:

$$m/\Delta m = \tau/2\Delta\tau \tag{7}$$

measured at some fraction of the peak height, typically FWHM or 10%.

5. ICBS Design

The calibration system (Figure 7) was comprised of a duoplasmatron ion source, beam-forming and acceleration optics, a 5 meter long grounded drift tube, two types of Faraday cups used to monitor beam current and uniformity, a 4-axis motion system that positioned and rotated CAPS in the ion beam, and an Ultra High Vacuum (UHV) chamber pumped by a combination of turbo-molecular and vac-ion pumps. In addition to the conventional pumps we added a liquid nitrogen cold plate kept at -120° C to increase pumping speed.
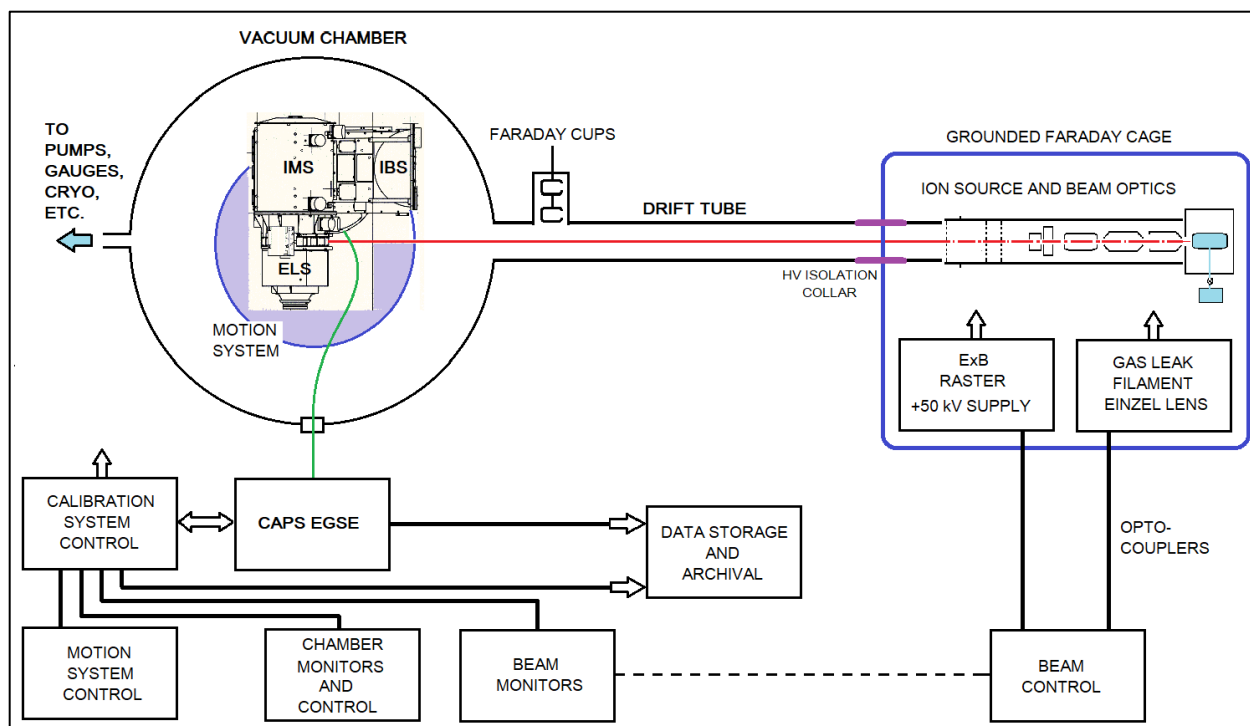
Figure 7. Schematic of the Ion Beam Calibration System (IBCS).

The ion source, optics and electronics were placed in a grounded wire-mesh Faraday cage that isolated all high voltages and source control equipment from ground potential (see photograph in Figure 8). The ion source and beam optics were biased by the beam acceleration high voltage supply. Although the system was designed to be capable of +50 kV and was tested up to ~40 kV, it was considered too much of a risk, and not essential for calibration, to operate continuously at those levels. Optical couplers were used to communicate across high voltage with the isolated source control electronics.

As indicated by the dashed line, there was no direct electrical connection between the ion source and beam monitoring equipment. While direct feedback is possible with a conventional electron ionization source, a plasma source runs at ~15 A. It is much more difficult to control and requires human intervention. Beam monitors (Faraday cups) and the chamber and motion system were controlled from a calibration system console. Data from the control and monitoring electronics were compiled and recorded in synch with CAPS data coming from the Electrical Ground Support Equipment (EGSE). This made it possible to store and compile results from all instrument tests and operations as well as goniometer angle data used for passband measurements.

Figure 8. IBCS high voltage Faraday cage with ion source inside. The vacuum chamber is at the far end of the room in this photo.

5.1 Ion source

The ion beam was created using a duoplasmatron ion source (PS-100 Peabody Scientific) together with beam extraction, shaping, and acceleration optics (Figure 9). The duoplasmatron source was chosen for its high output (current densities up to 1 pA/cm^2 = 10^{-12} A/cm^2 equivalent to 4 x 10^6 ions/cm^2/s) needed for useful counting rates for minor ion species such as fragments of methane (e.g., CH^+, CH_2^+, etc.). Since the beam diameter needed to fully cover one of the eight IMS apertures was ~5 cm, a raster system was used to vary beam diameter from ~1 cm to 5 cm. A maximum source output of ~20 pA was required to produce a density of ~1 pA/cm^2 over a 5 cm beam diameter. This is far larger than a conventional electron bombardment source can provide.

An extraction lens pulled ion current out of the dense plasma bubble that formed at the duoplasmatron exit aperture. Ions were then pre-accelerated to 1 keV inside the source optics (Figure 9) and focused on a 3500 Gauss ExB Wien mass filter. The filter had a resolution m/Δm ≈ 40 which was sufficient to separate mass species below ~20 with 1 amu resolution (Figure 7a). Energy resolution of the beam was $\Delta E/E \sim kT_D/1.0$ keV ~ 0.1% where kT_D is the thermal energy of ions leaving the source (~1 eV) and 1.0 keV is the pre-acceleration voltage.

ION SOURCE AND ACCELERATION OPTICS

HIGH VOLTAGE ISOLATION CAGE

DIFFUSION GRIDS   E x B MASS FILTER   EXTRACTION OPTICS

HV ISOLATION   X/Y DEFLECTION OPTICS   FOCUSING OPTICS   DUOPLASMATRON ION SOURCE

DRIFT TUBE

TO CALIBRATION CHAMBER (4 m)

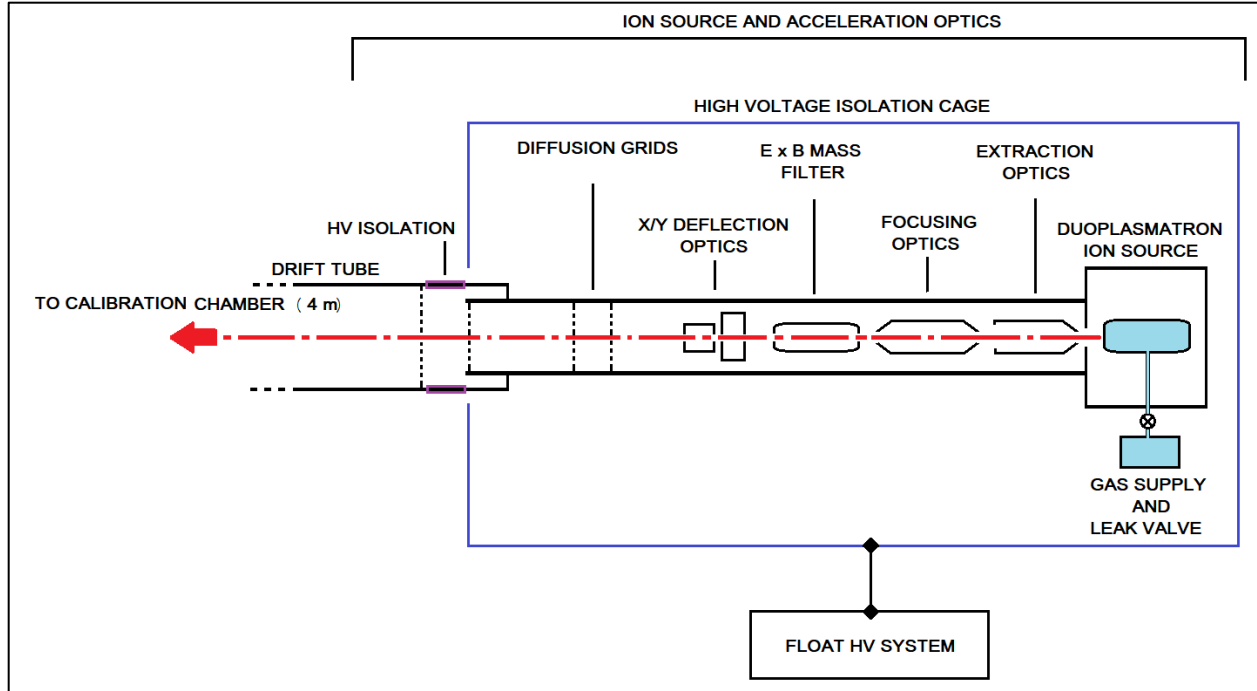GAS SUPPLY AND LEAK VALVE

FLOAT HV SYSTEM

Figure 9. Schematic of the ion source and beam acceleration optics.

Measuring IMS efficiency required relating the detector counting rate to the calibration beam current density I (A/cm^2) as a function of beam energy and species:

$$\varepsilon = q\, z\, C/\Delta t\, G\, I \tag{8}$$

where q = 1.60 x 10^{-19} coulombs, z is the ion charge state, and Δt the accumulation interval (typically 0.0625s for IMS but set here to 1s). Beam current calibration was performed each time the beam energy or species was changed and each time IMS was at the center of rotation looking into the beam direction ($\alpha = \beta = 0$).

Accurate control and measurement of beam current is critical and is one of the most challenging parts of calibration. The amount of beam current required for a given counting rate is

$$I = q\, z\, C/G\, \varepsilon \tag{9}$$

For IMS G = 1.5 x 10^{-3} cm^2 sr eV/eV. The efficiency of the TOF ST system $\varepsilon \approx 0.25$. LEF efficiency relative to ST varied with species and energy but was between ~4 and ~100 times less. Using these numbers the necessary beam current density could be estimated. For 1 kHz counting rate in the ST detector we require:

$$I_{ST} = 1.6 \text{ x } 10^{-19} * 1000/1.5 \text{ x } 10^{-3} * 0.25 = 4.3 \text{ x } 10^{-13} \text{ A/cm}^2 \tag{10}$$

For 1 kHz counting rate in the LEF we may need as much as ~4.3 x 10^{-11} A/cm^2. However in practice beam currents were kept at or below 10^{-12} A/cm^2 and instead the accumulation interval for LEF spectra was increased up to several minutes to reach the desired integral number of counts.

Beam current could be controlled in three ways. Increasing raster voltage dispersed the beam thereby lowering the current/area—this was the primary method. Current could also be changed by increasing the gas leakage rate, or by changing the duoplasmatron filament current. Both of the latter two methods then required tens of minutes for the beam to stabilize.

5.2 Beam formation and acceleration

After pre-acceleration inside the source, the beam passed through deflection plates that lined the focal point up with the remainder of the optics and applied triangular wave forms to raster the beam up to as much as ~5 cm diameter. The beam then went through a series of diffusion grids to ensure beam uniformity before it entered the final acceleration field.

A ceramic collar 20 cm long separated the drift tube, which was at ground potential, from the ion source and optics (Figure 9). The collar provided HV isolation so that an acceleration voltage of up to ~50 kV could be applied to the ion source and optics. For safety reasons the source and optics were placed in a grounded Faraday cage. All low voltage electronics within the cage were isolated from external ground to avoid arcing across the acceleration potential. Beam electronics inside the cage were controlled remotely across opto-couplers.

Once shaped and accelerated the beam traveled down a 5 m long x 25 cm diameter grounded drift tube. The purpose of the long drift tube was to allow off-axis velocity components to drift out of the beam thus increasing parallelism. At its exit from the source the beam aperture was 1 cm diameter so the 5 m drift tube collimated the beam to ~1/500 radians ~ 0.11°. This was much smaller than the smallest planned scanning pixel $\delta\alpha$ (0.5°).

Ions were accelerated to energies corresponding to 19 voltage steps out of the standard energy program of 63 log-space intervals. Although the full IMS range was ~1 eV to 50 keV it was advantageous to use a smaller range (1.024 to 27.56 keV) which was safer and simplified calibration procedures as well (27.56 kV is much easier to manage than 50 kV).

The reason we could skip the lower and upper ends of the energy range has to do with IMS optics. Ions leaving the ESA are accelerated by 14.56 kV before entering the TOF optics. This boost in energy allowed ions as low as ~1 eV external to the IMS to penetrate the carbon foils used in the TOF. With 14.56 kV acceleration the trajectories of ions between 1 eV and ~ 1 keV are virtually identical inside the TOF. The same is true for detection efficiencies: ~15 keV and ~16 keV ions are indistinguishable. By the same token, trajectories and efficiencies for ions approaching the upper end of the IMS energy range are nearly identical, allowing us to set the upper IMS calibration energy limit to 27.56 keV (~42.12 keV internal energy, well past the peak in electron emission). (The seemingly peculiar choice of energies corresponds to log-spaced energy steps programmed into the IMS HV supply.)

While keeping the beam energy constant the passband $\Delta E/E$ was scanned by micro-stepping the ESA plate voltage rather than stepping the beam voltage. The former was easy to do while the latter would have been impractical because other beam parameters such as raster scan and focus would have to be adjusted multiple times. The result of scanning ESA plate voltage is equivalent

to scanning beam energy since $\delta V/V_{ESA} = \delta E/E$ and $E = kV_{ESA}$ where k is the analyzer constant determined in calibration. The micro-step size was ~5% of $\Delta V/V$.

5.3 Beam monitoring

Beam intensity (in A/cm^2) was measured using two methods, both based on doubly-shielded Faraday cups (FCs). The FC_I measured current I directly using a Keithly pico-ammeter with a noise floor of 0.01 pA (= 10 fA = 10^{-14} A). The FC_{MCP} had a MCP with the same optical geometry. Both current monitors had 1.00 cm^2 aperture areas.

The idea behind the MCP FC was that at the low current end of the of the FC_I electrometer range (~30 fA/cm^2) the MCP was more sensitive and provided more accurate measurements as low ~10^2 ions/cm^2 s, equivalent to ~2.3 x 10^{-17}A/cm^2. The direct current measurement was considered the gold standard since it could be traced back to NIST if need be. Cross-calibration of the two was important and is shown in Figure 10 with the calibration equation:

$$FC_I \text{ (pA/cm}^2) = 0.25 \text{ } FC_{MCP} \text{ (kHz)} - 2.09 \text{ (pA/cm}^2). \tag{11}$$

FC current vs. MCP FC counts
6/24/1997, 16.4 keV, N+

IFC = 0.25 CFC (kHz) - 2.09 (fA)
R^2 = 0.8905

(y-axis) FC current (fA)
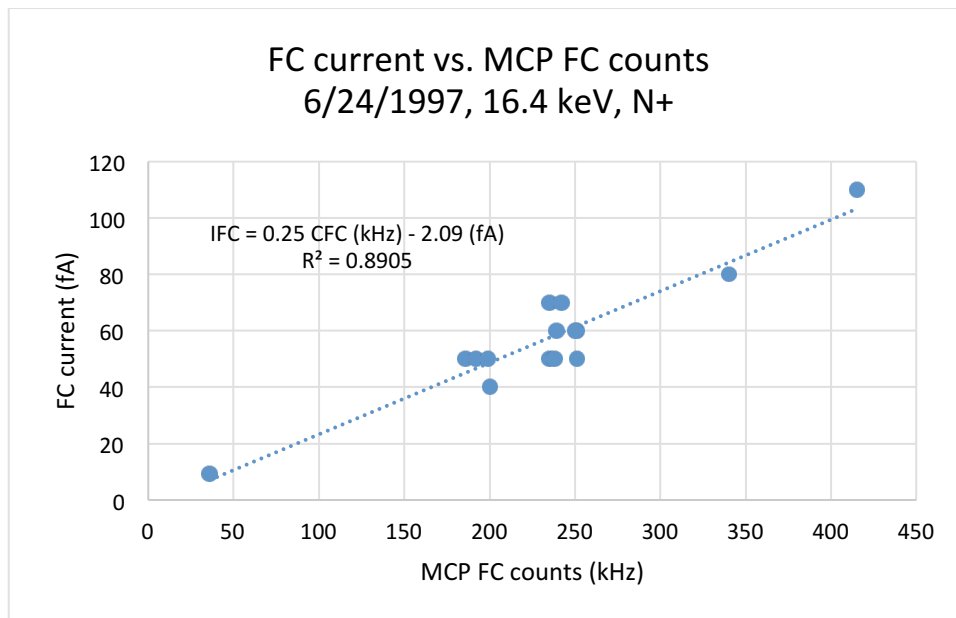(x-axis) MCP FC counts (kHz)

Figure 10. Plot showing the cross-calibration of FC current vs. MCP FC counting rate.

Beam energy. A high resolution ($\Delta E/E = 0.5\%$) cylindrical electrostatic analyzer beam monitor was developed specifically for IMS calibration. It was mounted on the motion system and moved into the beam to calibrate energy and energy spread. The optical design was very conservative and was calibrated based on numerical simulations and self-consistent cross-calibrations between the ESA, IBS and IMS.

Beam composition was one of the most critical elements of calibration. Composition was controlled by leaking a variety of gases into the ion source and then passing the resulting beam through the ExB mass filter. Figures 11a and 11b show mass spectra of the beam taken by the MCP FC with the raster off (Figure 11a) and with the raster set to maximum of 5V x 5V (Figure 11b). The MCP saturated on the dominant N_2^+ peak at ~2.5 MHz equivalent to 0.63 pA.
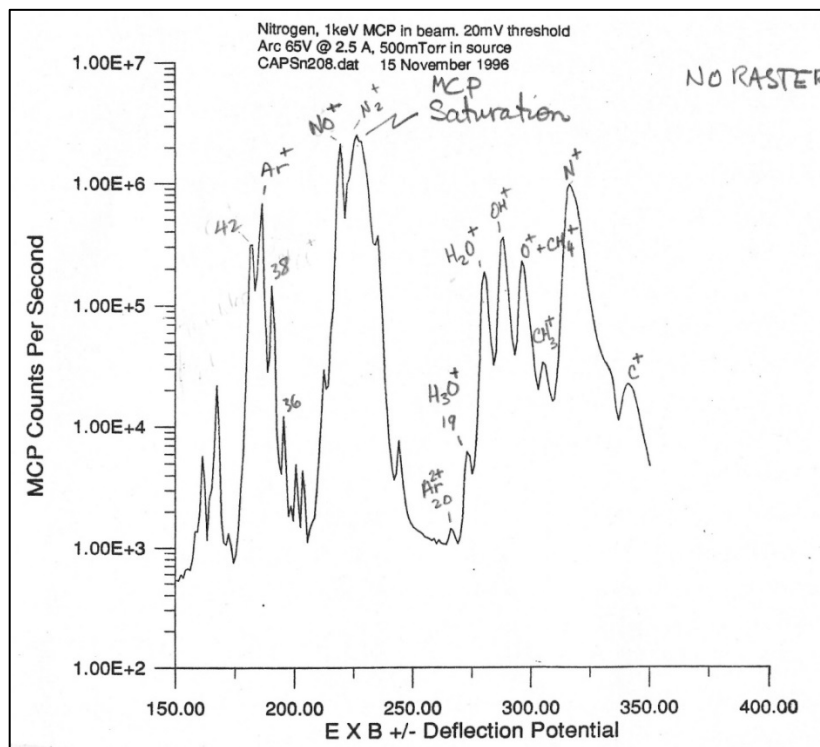

Figure 11a. Mass spectrum of ion beam taken with the MCP Faraday cup with no raster. The figure was taken from the IMS calibration log book.
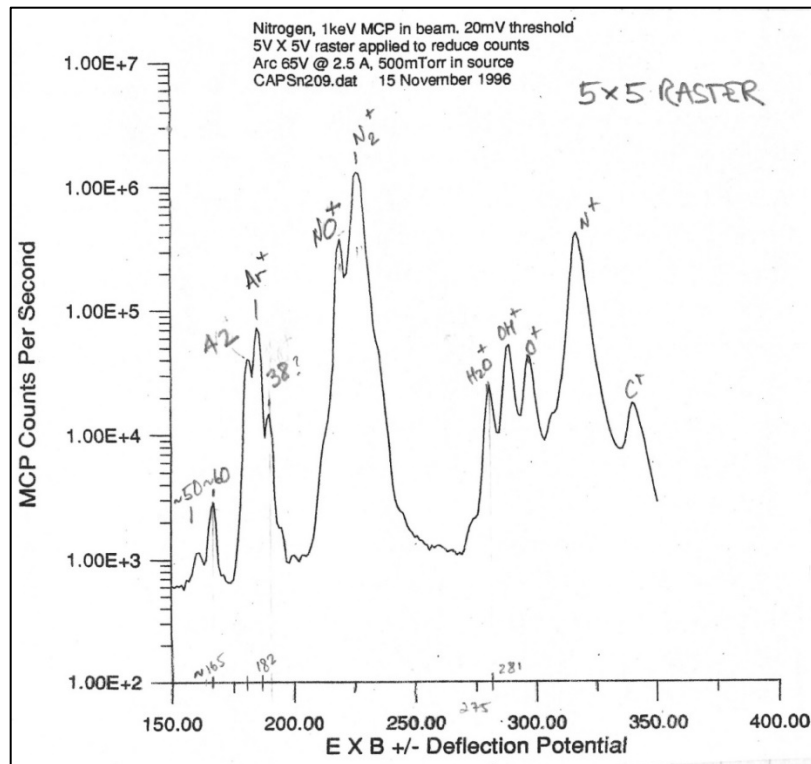
Figure11b. Mass spectrum of ion beam taken with the MCP Faraday cup with maximum raster. The figure was taken from the IMS calibration log book.

Figure 11a shows 1 amu resolution at 1% of peak height up to ~30 amu/q, more than adequate for IMS calibration purposes. With the raster on at maximum beam spread there is still 1 amu resolution up to ~18 amu/q (Figure 11b). Since high raster scans were only used to control the most intense peaks (N_2^+), most calibration spectra were taken with no raster thereby giving unit resolution up to 30 amu/q. The species used for calibration (Table 2) were primarily methane and ammonia products as well as oxygen, nitrogen, neon, and argon. (At GSFC hydrocarbon compounds C_xH_x such as acetylene (C_2H_2) were used in calibration.) The IBCS ExB mass spectrometer could not distinguish equal mass/charge ions such as 14 amu/q (CH_2^+, N^+) and 16 amu/q (O^+, CH_4^+, NH_2^+). However their relative abundances could be controlled by introducing the gases that would produce the desired composition, e.g., methane vs. ammonia.

Spatial distribution. In addition to measuring beam current, the FC_{MCP} gave a one-dimensional profile of the beam as it was moved vertically into and out of position. The beam was typically uniform to within 10% out to 90% of its width. The vertical profile could not be measured but was assumed to be similar based on design of the source optics.

5.4 Motion system

CAPS was mounted on a 4-axis motion system consisting of a 2-axis goniometer used to measure angular passbands, and a 2-axis translation table used to center the CAPS IMS and IBS apertures in a plane perpendicular to the beam direction (Figure 8). The system also moved ELS into the field-of-view of an electron source.
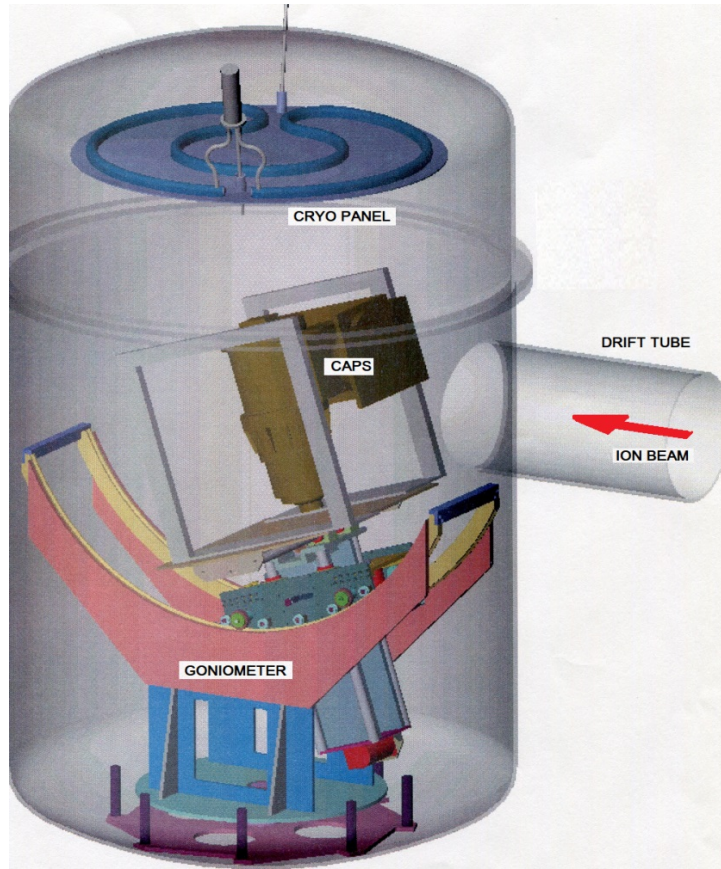
Figure 12. 3-D schematic of the 4-axis motion system. Ion beam enters from lower right.

The FOVs of IBS and IMS were centered separately on the beam line and then rotated about the center of the respective apertures. ELS was stimulated by an electron source mounted off the beam center. (Note that because of naming conventions and the orientation of CAPS on the goniometer, the CAPS elevation direction corresponds to the goniometer azimuth and CAPS azimuth corresponds to goniometer elevation (Figure 12). In this paper we use CAPS body coordinates.)

The goniometer could be programmed to rotate in steps corresponding to ~5% of the width of the respective passbands: $\Delta\alpha = 8.3°$ so $\delta\alpha = 0.5°$, and $\Delta\beta = 20°$ per sector so $\delta\beta = 1°$. Although a few high resolution scans were performed to get details of the passbands, most were done with 2° steps in both axes. Beccause they were only weakly dependent on energy, angle passbands were taken at only 5 external energies (1.024, 4.096, 9.74, 16.39, and 27.56 keV). These were chosen because the total energy inside the IMS (approximately 15.6, 18.7, 24.3, 31.0, and 42.1 keV) were spread roughly equally across the internal range.

5.5 Vacuum chamber

Design and fabrication of the IBCS vacuum chamber (Figure 13) was an important consideration because the base operating pressure was critical to instrument safety (e.g. a pressure surge could cause HV breakdown in the sensors) and instrument cleanliness. In addition the chamber volume and pumping speed affected the amount of time available for calibration.

Figure 13. 3-D schematic of the main chamber showing CAPS mounted on the 4-axis motion table. The cryo panel is located at the top of the chamber.

The ICBS chamber was designed to accommodate the fully integrated CAPS instrument which occupied a static volume of ~4 cubic feet. Figure 14 is a photograph of CAPS mounted on the motion system in the chamber prior to final calibration. The dynamic volume, i.e., the volume needed for the instrument to clear any obstructions while moving in the chamber, was ~8 cubic feet. The dynamic volume drove the size of the chamber (~4 ft. in diameter, 6.5 ft. high, ~ 80 cu. ft. volume), and hence the amount of pumping needed. In order to avoid electrical breakdown of the ±15 kV high voltages the chamber was kept at a working pressure $< 3 \times 10^{-8}$ Torr during calibration. This low pressure had to be maintained with the instrument dissipating ~20 W, which was enough heat to drive outgassing from internal surfaces and any virtual leaks that might trap gas internally. A roughly 7 sq. ft. liquid nitrogen (LN2) cold plate cooled to -120° C was added at the top of the chamber to speed pumping.
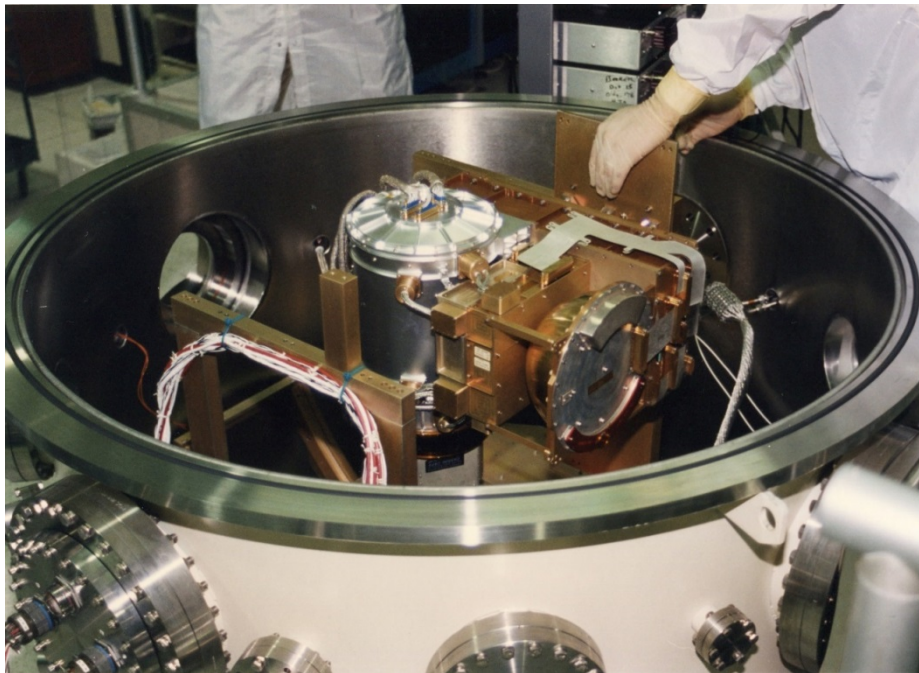

Figure 14. The Flight Model CAPS being mounted in the IBCS for final calibration.

6. IBCS Operation

The IBCS vacuum chamber was located in a clean tent with HEPA air filters and was kept under continual nitrogen purge when not under vacuum. The effect of the cryo panel on chamber cleanliness can be seen in residual gas analyzer (RGA) scans taken during a typical pump down sequence following bake out of CAPS to +55° C using the instrument's internal heaters.
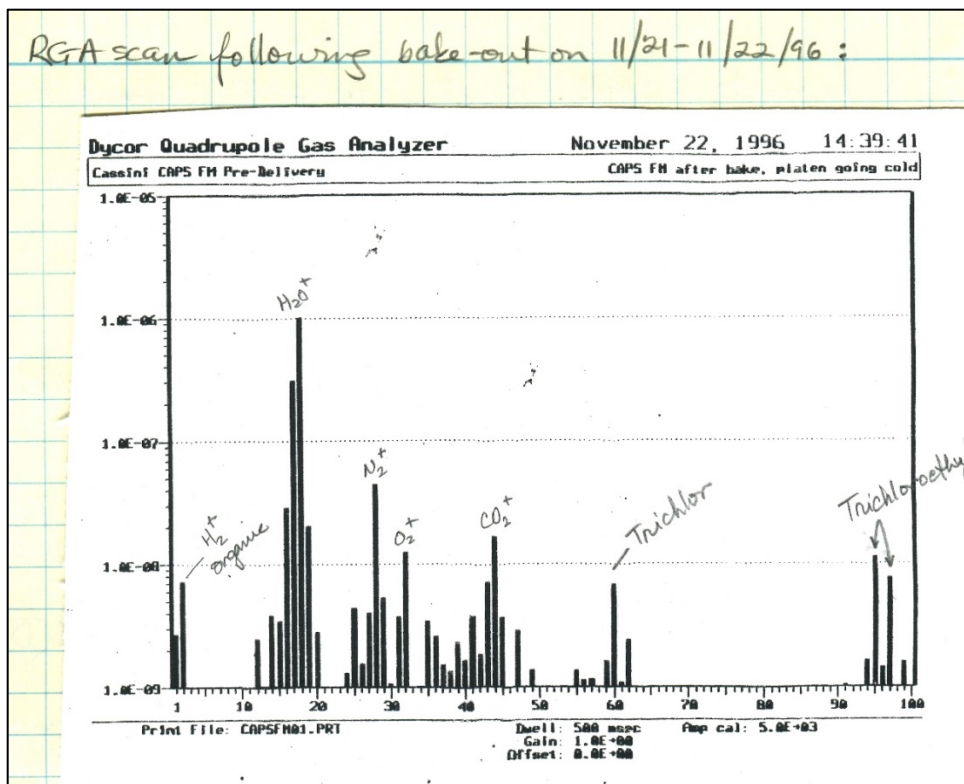
Figure 15a. RGA scan of vacuum chamber residual gases at 1.4 x 10⁻⁶ Torr. The figure was taken from the IMS calibration log book.

Figure 15a shows the system prior to cryo-panel turn-on at a pressure of 1.4×10^{-6} Torr. Figure 15b shows the system 24 hours later with the cryo-panel at -85° C and the pressure at 9.0×10^{-8} Torr. By then organic compounds from cleaning materials and plasticizers in the instrument were frozen out and/or pumped away. The remaining molecules are representative of background in a normal clean vacuum chamber, e.g., water is dominant. In practice, after ~1 week of pumping and with the cryo-panel operating at -120° C, the pressure when operating IMS HV at full power was $< 3.0 \times 10^{-8}$ Torr.
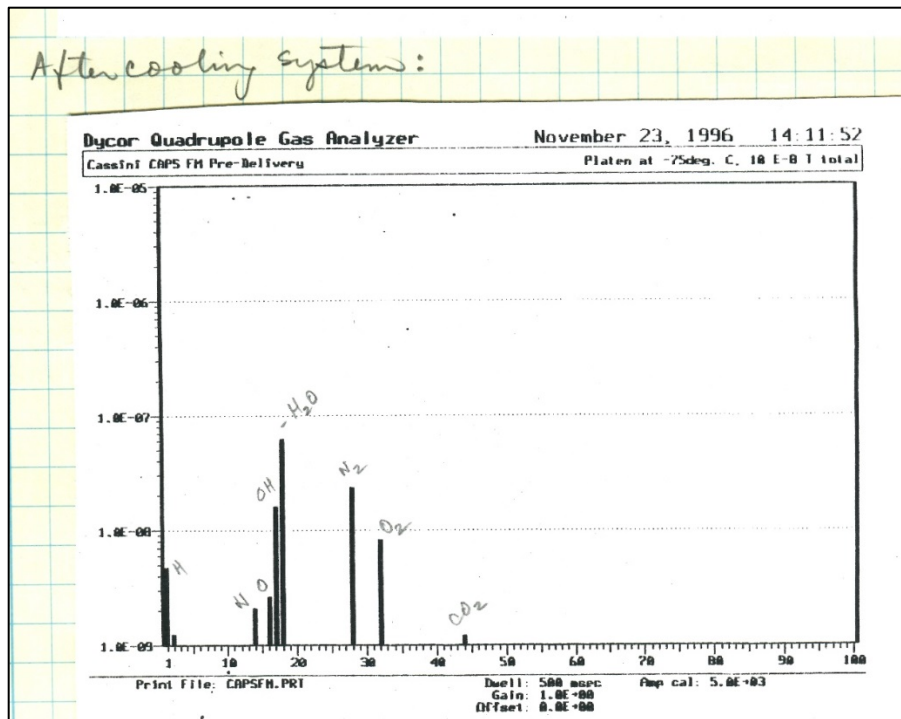
Figure 15b. RGA scan of vacuum chamber residual gases at 9.0 x 10^{-8} Torr. The figure was taken from the IMS calibration log book.

A calibration run typically started once chamber pressure reached ≤3 x 10^{-8} Torr with CAPS operating. Bringing CAPS voltages up into an operational state took between 4 and 12 hours depending on the length of time CAPS had been under vacuum.

Initially the ion source and drift tube were closed off from the main chamber by a gate valve. This allowed the beam and source to be pumped separately from the main chamber holding CAPS because the source and drift tube reached pressures a factor of ~30 higher than the main chamber. While the IMS HV was being brought up to operational levels, the ion source filament was warmed up and the gas leak was started in order to give the source time to stabilize. Once the source was ready the beam was prepared for operation by setting the ExB voltage and acceleration voltages. The deflection plates were then used to locate and raster the beam. Finally, the Faraday cup monitors were deployed to check beam properties. Changes in beam composition or energy during calibration runs usually required re-tuning the beam using the FC current as a monitor to relocate the beam and check uniformity, current, and composition.

CAPS was programmed to turn on in a low voltage state with all HV supplies shut off and armed. Once low voltages and basic digital operations were confirmed the HV supplies were brought up manually one at a time beginning with MCPs, the ESA, and then the TOF ±15 kV. Typically the initial HV turn on process following exposure to atmospheric pressure required ~24 hours (similar to what was used initially in flight). After a week of calibration the HV could be brought in as little as 4 hours. All HV operations were performed manually.

Once up and operating CAPS was programmed for whatever calibration program was scheduled and operated through the EGSE. This typically involved setting discrimination levels, MCP voltages, the length of accumulation cycles, energy levels and ESA micro-stepping values. Goniometer scans were programmed based on the range of angles and resolution desired. The goniometer and CAPS cycles were synched so that the cycles operated together, and data from both were transferred in files identified by scans and noted in log books. Beam current, gas leak, ExB settings, pressure, etc. were recorded in separate log books.

7. Results

Table 3 is a summary of final pre-flight calibration results for IMS and IBS. Although a simple electron source was built for ELS it was used only for functional tests of HV supplies and ESA operation. (See Young et al., 2005, Table VII for a summary of all CAPS calibration results.)

Table 3. IMS and IBS calibration results.

Calibration Parameter	IMS ST (SNG)	IMS LEF	*IBS
Energy range calibrated (keV)	0.25 – 27.56	0.25 – 27.56	1.024-25.0
Energy resolution ($\Delta E/E$ FWHM)	0.17	0.17	0.013
Analyzer constant ($\Delta V/V_{ESA}$ FWHM)	6.3	6.3	19.4
Azimuth FWHM	8.3°	8.3°	1.4°
Elevation FWHM	20°	20°	1.4°
Mass range (m/q)	0.3 - 400	0.1 - 54	N/A
Mass resolution (m/Δm FWHM)**	≤ 5	≤ 40	N/A
Mass resolution (m/Δm @ 10% of peak)**	≤ 15	≤ 85	N/A
Geometric factor (cm2 sr eV/eV)	1.5 x 10-3	1.5 x 10-3	7.5 x 10-5
Detection efficiency (counts/ion)***	0.266	~0.05	0.31

*IBS data are from calibration in the IBCS. For final values see Young et al., 2005, Table VII.
** Values are maximum resolution at 9.74 keV for ST species C[-] and LEF species ^{20}Ne[+].
*** Taken with N[+] at 16.4 keV.
N/A = not applicable.

The dependence of TOF peak shapes and spectra on incident angle and energy is an important issue that is difficult to quantify for all species and energies. However it is possible to demonstrate with calibration data that key assumptions about instrument performance can be verified. Figure 16 demonstrates focusing across the $\Delta\alpha$ passband at 2° intervals (α is the focusing plane for ESA optics). In addition, at each azimuthal step a micro-stepping voltage scan was made across the energy passband ($\Delta E/E$). Note that in the figure all TOF spectra fall within a single envelope with very little or no broadening. This demonstrates angle-energy focusing as well a lack of scattering in the foils that might otherwise broaden TOF peaks.
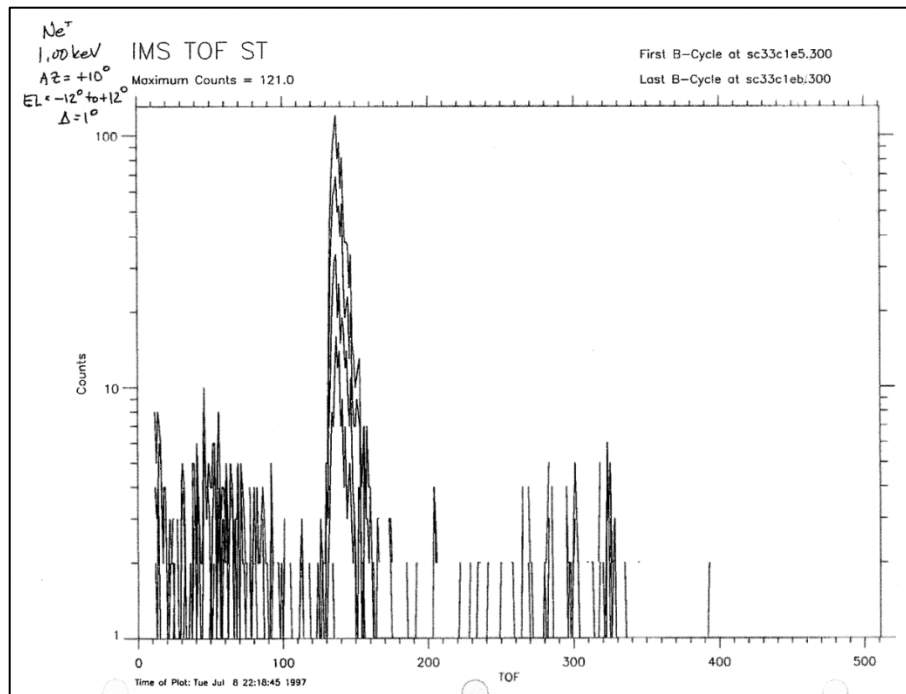
Figure 16. An overlay of ST spectra taken every 2° in azimuth from -12° to +12°.

Figure 16 gives some confidence that although TOF calibration of the PT IMS post-launch at GSFC made use of an uni-directional, mono-energetic beam, the peaks most likely are not much narrower than they would be in a space plasma environment.

One other important property of the TOF optics that was expected, but not to the extent observed in calibration, was the complexity of spectra from even simple molecules. The complexity is the result of molecular fragments with different charge states plus the presence of energy-dependent ghost peaks. Figure 17 shows one example of a LEF spectrum taken at 19.49 keV with an NH_2^+ beam. At this energy positive ions can only reach the LEF detector as fragments with energies less than ~17 keV.

The primary peak in Figure 13 is N^+ and the large peak at short times is H^+. The three sharp peaks to the left of the main peak and the peak to the right are positively charged fragments. The fact that they are sharp demonstrates that they are in focus as expected for the LEF optics. The two broad peaks between H^+ and N^+ are ghosts from scattered fragments. This spectrum is just one example of many from calibration of molecular species. It has not been reduced to become part of the TOF library. However it does show the complexity of TOF spectra and hints at the amount of effort it would take to do that reduction.
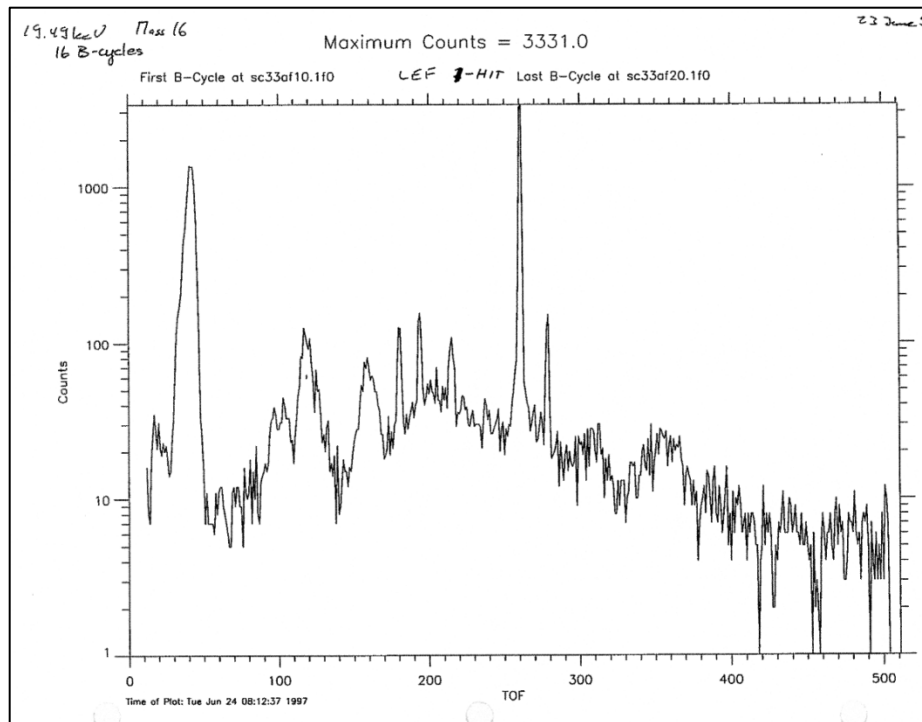
Figure 17. LEF spectrum of NH$_2^+$ at 19.49 keV.

Figure 18 is an example of simpler spectra that can easily be used in a library. The larger ST peaks in Figure 18 represent negatively charged and neutral water fragments. The smaller peaks at far left are hydrogen fragments. The left LEF peak consists of H$^+$ water fragments while the far right peak is made up of O$^+$ fragments. A characteristic of all TOF spectra is the small ratio of LEF to ST ions reflecting the low efficiency caused by the multiplicity of contributing factors (cf. Equation 4).

8. Lessons learned

A number of problems crept up that delayed calibration and reduced the amount of data that could be taken. These form the basis for several lessons learned.

The first problem, which was inescapable once the IMS design was frozen and built, was that spectrometers based on carbon foils could be far more complex than anticipated. Ray tracing and limited experience with simpler prototypes did not really indicate the difficulties, such as fragments and ghost peaks, which would be encountered in flight spectra. More extensive pre-flight calibrations would have been extremely helpful. Unfortunately, although 3 months had been allocated for flight calibration (April – June, 1997), production problems arose with the HVU 1 supply that generated ±15 kV. The supply was removed and reworked expensively at GSFC. IMS and CAPS were re-integrated in mid-May and mounted in the calibration chamber on May 24, 1997. Operating pressure was reached on June 3 at which point the HV supplies could be brought to full voltages. Thermal vacuum tests, which also served as sensor bake-out, took place through June 15. Calibration with the ion beam began on June 16 and lasted through

July 9—a total of 24 days during which the calibration team averaged 18 hours/day and often pulled 24 hour shifts. The loss of ~10 weeks of calibration time had serious repercussions for the IMS, leading to the need for extensive in-flight and post-flight calibration.

The most common operational problems were sudden drops ("knockdowns") of the ±15 kV supplies. Since the supplies were monitored internally, any voltage fluctuation above a pre-set level caused the supply to step down to safe levels. Knockdowns were typically characterized by a burst of high counting rates but surprisingly the IMS TOF system did not seem to suffer any damage. The problem was identified as micro-discharges caused primarily by cleanup of dust particles from charged internal surfaces. Less common were beam problems with power supplies or filaments.

A fairly obvious, system-wide, and nearly continuous problem was that CAPS and the IBCS had never been operated together before. The IBCS source and optics, the motion system, and the LN2 cold plate were all new and were developed in the same time frame that the CAPS EGSE and EGSE software were coming together. In addition calibration was the first time that the IMS had been operated for any length of time in an ion beam with the capabilities of IBCS. Initial results with molecular spectra were surprising and took some time to understand, even if only imperfectly. As the data rolled in we had to revise plans constantly to take into the account the complex nature of the TOF spectra and their energy and species dependencies. It is not clear that all IMS characteristics could have been anticipated, but the 10 weeks of time lost to repairing HV supplies would have made a big difference.

CAPS was removed from the IBCS on July 10 and shipped to Cape Canaveral for integration on the spacecraft July 16. Final closeout was completed when the IMS cover was latched on August 8. Cassini launched on Oct. 15, 1997 and the IMS saw first light in the solar wind on Jan 10. 1998.

.